



NRL/MR/6110--12-9400

# Quantification of Noise Sources in EMI Surveys

## ESTCP MR-0508

### Final Guidance Document

GLENN R. HARBAUGH  
DANIEL A. STEINHURST  
*Nova Research, Inc.*  
*Alexandria, Virginia*

MARK J. HOWARD  
*NAEVA Geophysics, Inc.*  
*Charlottesville, Virginia*

BRUCE J. BARROW  
JONATHAN T. MILLER  
THOMAS H. BELL  
*SAIC, Inc. - ASAD*  
*Arlington, Virginia*

April 9, 2012

Approved for public release; distribution is unlimited.

# REPORT DOCUMENTATION PAGE

*Form Approved*  
*OMB No. 0704-0188*

Public reporting burden for this collection of information is estimated to average 1 hour per response, including the time for reviewing instructions, searching existing data sources, gathering and maintaining the data needed, and completing and reviewing this collection of information. Send comments regarding this burden estimate or any other aspect of this collection of information, including suggestions for reducing this burden to Department of Defense, Washington Headquarters Services, Directorate for Information Operations and Reports (0704-0188), 1215 Jefferson Davis Highway, Suite 1204, Arlington, VA 22202-4302. Respondents should be aware that notwithstanding any other provision of law, no person shall be subject to any penalty for failing to comply with a collection of information if it does not display a currently valid OMB control number. **PLEASE DO NOT RETURN YOUR FORM TO THE ABOVE ADDRESS.**

<b>1. REPORT DATE (DD-MM-YYYY)</b> 09-04-2012		<b>2. REPORT TYPE</b> Memorandum Report		<b>3. DATES COVERED (From - To)</b> April 2006 - April 2010	
<b>4. TITLE AND SUBTITLE</b>  Quantification of Noise Sources in EMI Surveys ESTCP MR-0508 Final Guidance Document				<b>5a. CONTRACT NUMBER</b>	
				<b>5b. GRANT NUMBER</b>	
				<b>5c. PROGRAM ELEMENT NUMBER</b> 0603851D8Z	
				<b>5d. PROJECT NUMBER</b> MM-0508	
<b>6. AUTHOR(S)</b>  Glenn R. Harbaugh,* Daniel A. Steinhurst,* Mark J. Howard,† Bruce J. Barrow,‡ Jonathan T. Miller,‡ and Thomas H. Bell,‡				<b>5e. TASK NUMBER</b>	
				<b>5f. WORK UNIT NUMBER</b> 61-5802-A-1-5	
				<b>8. PERFORMING ORGANIZATION REPORT NUMBER</b>  NRL/MR/6110--12-9400	
<b>9. SPONSORING / MONITORING AGENCY NAME(S) AND ADDRESS(ES)</b>  Naval Research Laboratory, Code 6110 4555 Overlook Avenue, SW Washington, DC 20375-5320				<b>10. SPONSOR / MONITOR'S ACRONYM(S)</b>  ESTCP	
				<b>11. SPONSOR / MONITOR'S REPORT NUMBER(S)</b>	
<b>12. DISTRIBUTION / AVAILABILITY STATEMENT</b>  Approved for public release; distribution is unlimited.					
<b>13. SUPPLEMENTARY NOTES</b> *Nova Research, Inc., 1900 Elkin Street, Suite 230, Alexandria, VA 22308 †NAEVA Geophysics, Inc., P.O. Box 7325, Charlottesville, VA 22906 ‡SAIC, Inc. - ASAD, 4001 N. Fairfax Drive, 4th Floor, Arlington, VA 22203					
<b>14. ABSTRACT</b>  A series of field measurements were made under carefully controlled conditions at our home facility at the Army Research Laboratory Blossom Point Facility between July and September 2006. The magnitudes and effects of several types of background and noise sources on the data collected with several commonly used EMI sensors were measured. These noise sources included ground response/geology, inherent sensor noise, external noise sources, motion-induced noise, and position uncertainty. By use of Monte Carlo simulations of the fitting process for a canonical object using the collected data, the impact of each noise source on the final fitted parameters result was determined and compared to a similar analysis done for the 4.2-in. mortar. Two recommendations are provided as to a set of EMI sensors and a demonstration protocol to be used for future demonstrations. We have attempted to quantify these effects in terms of survey configuration parameters that are under site manager and data collection operator control, such as lane spacing and survey mode.					
<b>15. SUBJECT TERMS</b>  Unexploded Ordnance (UXO)      Noise sources      Classification Electromagnetic induction (EMI)      Survey background levels      Discrimination					
<b>16. SECURITY CLASSIFICATION OF:</b>			<b>17. LIMITATION OF ABSTRACT</b>	<b>18. NUMBER OF PAGES</b>	<b>19a. NAME OF RESPONSIBLE PERSON</b>
<b>a. REPORT</b>	<b>b. ABSTRACT</b>	<b>c. THIS PAGE</b>			B.J. Spargo, NRL, Code 6110
Unclassified Unlimited	Unclassified Unlimited	Unclassified Unlimited	Unclassified Unlimited	64	<b>19b. TELEPHONE NUMBER (include area code)</b> (202) 404-6392



# Contents

Figures.....	vi
Tables.....	ix
Acronyms Used.....	xi
Acknowledgements.....	xiii
Executive Summary.....	E-1
1. Introduction.....	1
1.1 Background.....	1
1.2 Objectives of the Project.....	1
1.3 Regulatory Drivers.....	2
1.4 Stakeholder / End User Issues.....	2
2. Technology Description.....	2
2.1 Technology Development and Application.....	2
2.1.1 Geophysical Instruments.....	2
2.1.1.1 Geonics EM61 MkII.....	2
2.1.1.2 Geonics EM63.....	4
2.1.1.3 Geophex GEM-3.....	4
2.1.1.4 Position and Orientation.....	6
2.1.2 NRL Low Frequency Spectrum Analyzer.....	6
2.1.3 Test Platforms.....	7
2.2 Advantages and Limitations of the Technology.....	8
3. Demonstration Site.....	9
3.1 Test Site Selection.....	9
3.1.1 Test Site History / Characteristics.....	9

3.1.2	Climate.....	10
3.1.3	Geology.....	10
3.1.4	Test Locations within Blossom Point.....	11
3.1.4.1	Environmental Area.....	11
3.1.4.2	Boat Launch.....	11
3.1.4.3	L Range.....	12
4.	Noise Source Analyses.....	13
4.1	Inherent Noise of Geophysical Sensors.....	13
4.2	External Noise Sources.....	16
4.3	Motion-Induced Noise.....	19
4.4	Characterization of the Soil by Standard Techniques.....	25
4.4.1	Soil Moisture.....	25
4.4.2	Magnetic susceptibility of soils.....	26
4.5	Response to Ground.....	27
4.6	Geolocation Uncertainties.....	33
4.7	Blossom Point, MD – An Example Noise Budget.....	34
5.	Monte Carlo Study.....	36
5.1	Objective.....	36
5.2	The Monte Carlo Approach.....	36
5.3	Modeling an EMI Survey Scenario.....	37
5.4	Stochastic Model.....	37
5.5	Simulation Results.....	38
6.	Implementation at a New Site.....	42
6.1	Full-Scale EMI Noise Characterization Demonstration.....	42

6.1.1	EMI Sensors.....	42
6.1.2	Measurements .....	45
6.1.3	Deliverables .....	45
6.2	EM61 MkII Simulation Tool Demonstration .....	45
6.2.1	EMI Sensors.....	45
6.2.2	Measurements .....	46
6.2.3	Deliverables .....	46
7.	References .....	47
8.	Points of Contact .....	49

## Figures

Figure 2-1 – Geonics EM61 MkII coils on a test platform.....	3
Figure 2-2 – Geonics EM63 with electronics and data logger, on a test platform .....	4
Figure 2-3 – Geophex GEM-3 sensor head (40cm diameter) and electronics.....	5
Figure 2-4 – NRL Low-Frequency Spectrum Analyzer .....	7
Figure 2-5 – Man-portable cart.....	7
Figure 2-6 – Rail system and test tower.....	8
Figure 2-7 – MTADS EM trailer .....	8
Figure 3-1 – Location of Army Research Laboratory Blossom Point Facility.....	9
Figure 3-2 – Topographic Map of Blossom Point Research Facility, showing locations of selected EMI Noise test sites .....	10
Figure 3-3 – Environmental Area, view to the East.....	11
Figure 3-4 – Boat Landing Area, view to the southwest .....	12
Figure 3-5 – Active Range Test Location, L-Range, view to the East .....	13
Figure 4-1 – A time raster plot of the in-phase and quadrature static response of the GEM-3 at 3,930 Hz. The in-phase and quadrature responses are shown in black and red, respectively.....	14
Figure 4-2 – Averaged power spectrum of the in-phase and quadrature static response of the GEM-3 at 3,930 Hz. The in-phase and quadrature responses are shown in black and red, respectively. The white noise floor is shown as a dashed line.....	14
Figure 4-3 – White Noise Levels for GEM-3 Static Measurements. Measurements at each transmit frequency are shown as symbols (black diamonds – in-phase, red x’s – quadrature). A polynomial fit to the data is shown as a dashed line.....	15
Figure 4-4 – Time Raster for time gate #1 of a Stationary EM61 MkII in a Quiet Location. ....	16
Figure 4-5 – Averaged Relative Power Spectra for a Stationary EM61 MkII in a Quiet Location. The dotted lines represent the channel-specific noise floor (bit	

level). The red curves plot the power spectral response as determined by the sensor's step response.....	16
Figure 4-6 – Power Spectra Results for the GEM-3 Sensor in both Passive (black) and Active (red) Monitoring Modes.....	18
Figure 4-7 – External Noise Relative Power Spectrum for vertically oriented EM61 receiver coil facing north at the Boat Launch Area.....	18
Figure 4-8 – Schematic drawing of an EMI sensor receive coil moving in the Earth's field.....	19
Figure 4-9 – IMU angular pitch rate versus the 90-Hz GEM-3 Response (In-phase and Quadrature).....	21
Figure 4-10 – Measured Response from an EM61 MkII while Undergoing Controlled Pitching. The top panel shows the sensor motion as measured by the IMU. The channel data are shown in the bottom panel as color-coded lines (time gates 1 – 4, magenta, blue, red, and green, respectively). The black line represents the modeled response using the IMU data.....	23
Figure 4-11 – Modeled and Measured EM61 MkII Response (for Various Pitching Rates. The channel data are shown as color-coded lines (time gates 3 – red and 4 - green). The black line represents the modeled response using the IMU data.....	24
Figure 4-12 – Moisture content profiles for the Boat Launch, Environmental, and L-Range areas.....	25
Figure 4-13 – Magnetic susceptibility profile for a) the Environmental Area, and b) the Boat Launch Area.....	26
Figure 4-14 – Magnetic susceptibility profile for the L-Range traverses.....	26
Figure 4-15 – Schematic drawing of an EMI sensor receiver coil moving across a ground surface.....	27
Figure 4-16 – Soil Model Response for the GEM-3 sensor. In-phase response is shown in red and quadrature response is shown in blue.....	28
Figure 4-17 – Soil Model Response for the GEM-3 sensor. In-phase response is shown in red and quadrature response is shown in black. The solid lines represent a soil conductivity of 0.01 mho/m, the dashed lines 0.1 mho/m.....	29
Figure 4-18 – Match of frequency dependent susceptibility model (red and green curves) to measured GEM-3 soil response (black curves and symbols) at the Environmental Area.....	30

Figure 4-19 – Time-Domain Soil Response Measured using the EM61 MkII in 4-channel mode as a function of measurement height. The experimental data are shown as color-coded symbols and lines. The dashed lines represent the soil model discussed in the text as a function of sensor height. ....32

Figure 4-20 – Time-domain soil response measured and modeled using single sensor from MR-0601 TEM array as a function of measurement height. The black lines are the experimental data and the green lines represent the model results. ....33

Figure 4-21 – Cross-track RMS variation of GPS position for a GPS position mounted on a rail system tower. ....34

Figure 4-22 – Vertical RMS variation of GPS position for a GPS position mounted on a rail system tower. ....34

Figure 4-23 – Noise budgets for the GEM-3 sensor at Blossom Point, MD for towed-platform and man-portable deployment configurations. The noise floor for a stationary GEM-3 are shown in black. ....35

Figure 4-24 – Noise budgets for the EM61 MkII at Blossom Point, MD for towed-platform and man-portable deployment configurations. The noise floor for a stationary EM61 MkII are also shown. ....36

Figure 5-1 – Contour maps of synthetic EM61-MkII data, first time gate. The raw data (left image) shows the characteristic “chevron” pattern caused by the delayed onset of peak signals due to dynamic response of the sensor, which is moving at walking speed (~1 m/s). In the right image, a time lag is applied to the raw data, effectively shifting positions along-track until contours appear by eye to be aligned properly for further processing. ....38

Figure 5-2 – Output from this Monte Carlo study (left two graphs) compares with corresponding results from Camp Sibert (right two graphs) in which a large number of 4.2-in mortars were processed. The upper set of graphs shows the relationship between fit error and signal to noise ratio (SNR). The lower set shows the spread of recovered beta values. This comparison is imperfect since the man-portable system deployed at the former Camp Sibert is different from the system modeled in this study (Figure 2-5). Still, the broad trends encourage a sense that these results are reasonable representations of reality. ....39

Figure 5-3 – Predicted performance with different lane spacings. The upper panels show the fitted z results and the lower panels plot  $\beta_2$  and  $\beta_3$  versus  $\beta_1$ . The solid line in the upper panels indicates where the fitted z equals the true z value. ....41

Figure 5-4 – Predicted performance for other survey configurations. The upper panels show the fitted z results and the lower panels plot $\beta_2$ and $\beta_3$ versus $\beta_1$ . The solid line in the upper panels indicates where the fitted z equals the true z value. ....	42
Figure 6-1 – MTADS Discrimination Array Transients for Several Items .....	43
Figure 6-2 – EMI sensor developed during ESTCP MR-0601 .....	44
Figure 6-3 – Handheld TEM sensor developed for ESTCP MR-0807 in the field.....	44

## Tables

Table 4-1 – Nominal EM61 MkII RMS Noise Characteristics and Digitizer Bit Levels.....	16
Table 4-2 – Fitted Soil Model Parameters for the Blossom Point Test Areas.....	31
Table 5-1 – Steps of the Stochastic model.....	37



## Acronyms Used

<b>Abbreviation</b>	<b>Definition</b>
(PTNL,)AVR	Time, Yaw, Tilt, Range for Moving Baseline RTK NMEA-0183 message
(PTNL,)GGK	Time, Position, Position Type, DOP NMEA-0183 message
AGL	Above Ground Level
APG	Aberdeen Proving Ground
BP	US Army Research Laboratory Blossom Point Facility, MD
DoD	Department of Defense
DSB	Defense Science Board
DVD-R	Writable digital versatile disc
EM(I)	Electro-magnetic (Induction)
ESTCP	Environmental Security Technology Certification Program
FFT	Fast Fourier Transform
GPS	Global Positioning System
HASP	Health and Safety Plan
Hz	Hertz
IMU	Inertial Measurement Unit
MM	Munitions Management
MP	Man-portable
MTADS	Multi-sensor Towed Array Detection System
NAD83	North American Datum of 1983
NAVD88	North American Vertical Datum of 1988
NMEA	National Marine Electronics Association
NRL	Naval Research Laboratory
ppm	parts-per-million
PSD	Power Spectral Density
RMS	Root Mean Squared
RTK	Real Time Kinematic
SERDP	Strategic Environmental Research and Development Program
SI	International System of Units
SNR	Signal to Noise Ratio
TEM	Time-Domain Electro-magnetic Induction
TFM	Total-Field Magnetometry
UTC	Universal Coordinated Time
UTM	Universal Transverse Mercator
UXO	Unexploded Ordnance
VHF	Very High Frequency



## **Acknowledgements**

ESTCP project MR-0508 “Quantification of Noise Sources in EMI Surveys” was a collaborative effort between the Naval Research Laboratory, Nova Research, Inc., Science Applications International Corporation (SAIC), and NAEVA Geophysics, Inc. Dan Steinhurst (Nova Research) was the Principal Investigator of this project. Glenn Harbaugh and Dan Steinhurst (Nova Research), Tom Bell and Bruce Barrow (SAIC), and Mark Howard and Brian Neely of NAEVA Geophysics collaborated on the data collection efforts. Tom Bell, Bruce Barrow, and Jonathan Miller (SAIC) were responsible for the modeling/analysis of the resultant data.

## Executive Summary

ESTCP project MR-0508, “Quantification of Noise Sources in EMI Surveys” consisted of a long-running series of field measurements made under carefully controlled conditions at our home facility at the Army Research Laboratory Blossom Point Facility between July and September 2006. The magnitudes and effects of several types of background and/or noise sources on the data collected with several commonly-used EMI sensors were measured. These noise sources included ground response / geology, inherent sensor noise, external noise sources, motion-induced noise, and position uncertainty. By use of Monte Carlo simulations of the fitting process for a canonical object using the collected data, the impact of each noise source on the final fitted parameters result was determined and compared to a similar analysis done for the 4.2-in mortar.

The Blossom Point site was found to be a relatively benign site for EMI sensor measurements and provides a good benchmark for a site where it should be feasible to conduct a survey-mode EMI survey. Two recommendations are provided as to a set of EMI sensors and a demonstration protocol to be used for future demonstrations. From these results, we can begin to understand real world EMI survey noise sources both individually and in combination. We also have attempted to quantify these effects in terms of survey configuration parameters which are under site manager and data collection operator control, such as lane spacing and survey mode.

The first strategy is a set of measurements and analysis based on the lessons learned from this project to be conducted on a new site over the course of a week. The results of these measurements would provide information to the site manager as to what sensors can be used and what information can be extracted for the site. The second strategy involves the planning tool, the EM61 MkII Simulation Tool, allows a site manager to visualize the impact of various noise sources *a priori* to collecting site-specific data for planning purposes. From these results, one can begin to understand real world EMI survey noise sources both individually and in combination. One can start to quantify these effects in terms of survey configuration parameters which are under site manager and data collection operator control, such as lane spacing and survey mode.

# Quantification of Noise Sources in EMI Surveys

## Final Guidance Document

### 1. Introduction

#### 1.1 Background

Unexploded Ordnance (UXO) detection and remediation is a high priority tri-service requirement. As the Defense Science Board wrote in 2003: “Today’s UXO cleanup problem is massive in scale with some 10 million acres of land involved. Estimated cleanup costs are uncertain but are clearly tens of billions of dollars. This cost is driven by the digging of holes in which no UXOs are present. The instruments used to detect UXOs (generally located underground) produce many false alarms, - i.e., detections from scrap metal or other foreign or natural objects -, for every detection of a real unexploded munition found.” [1]

There is general agreement that one solution to the false alarm problem involves the use of Electromagnetic Induction (EMI) sensors which can, in principle, allow the extraction of target shape parameters in addition to the size and depth estimates available from magnetometer measurements. We, and others, have fielded systems with either time-domain or frequency-domain EMI sensors with the goal of extracting reliable target shape parameters and, thus, improving the discrimination capability of our surveys. In practice, the discrimination ability of these sensors has been limited by signal-to-noise limitations. Part of this noise results from sensor design but a large fraction arises from causes external to the sensor such as location uncertainty, motion-induced noise, ground interaction, and external noise sources.

SERDP and ESTCP have funded several groups to develop ordnance-specific EMI sensors. Many of these groups are using simulations to investigate the performance of their prototype sensors in realistic environments. These simulations, along with those being conducted by algorithm developers, are limited by our lack of quantitative knowledge of the magnitude of the various noise sources. The results of this project can be used to develop a knowledge base of magnitude and variation of the noise budget associated with various EMI sensors, and how to guide the design of these surveys.

#### 1.2 Objectives of the Project

In this ESTCP-funded Naval Research Laboratory (NRL) project, we have isolated, to the extent possible, and measured quantitatively the individual components of the noise budget for an EMI survey. These components include inherent sensor noise, motion-induced noise, external noise, ground interactions, and location uncertainties. Each of these terms will be discussed in more detail below. The data collection was conducted at our home facility to accommodate an evolution of data collection schemes and techniques in response to the collected data, with a correspondingly long deployment schedule.

### **1.3 Regulatory Drivers**

DoD directives to develop new techniques and technologies to improve the efficiency of UXO cleanup at military training sites form the impetus for this study. Careful analysis of the sources contributing noise to EMI instrument readings will permit their effects to be anticipated and considered in the development and application of discrimination algorithms. As a result, cost savings will result from improved discrimination of UXO and non-UXO scrap at munitions sites.

We address this issue in two ways. The quantitative measure of EMI noise sources that resulted from this project are an important tool for both sensor and algorithm developers and should enable them to make real progress in the area of UXO classification. More directly, we have used our acquired knowledge of EMI noise sources to formulate simple tests that can be performed on-site before an EMI survey and whose result can be used to optimize analysis and classification algorithms to reduce the number of false alarms.

### **1.4 Stakeholder / End User Issues**

End users of the information derived from this study are the site managers and regulators who oversee the nation's Formerly-Used Defense Sites, the contractors who routinely conduct EMI surveys for the purposes of site investigation and clearance, and the algorithm developers working to improve discrimination techniques. The utility of our results to the UXO detection and discrimination community will depend on the extent to which they are disseminated. The publication of our final results and analyses in this document will help insure wide distribution in the archival literature.

## **2. Technology Description**

### **2.1 Technology Development and Application**

#### **2.1.1 Geophysical Instruments**

Three commonly used, commercially-available EMI geophysical instruments were used in this project to evaluate the primary noise sources affecting EMI sensors. The three instruments are the Geonics EM61 MkII and EM63 and the Geophex GEM-3.

##### **2.1.1.1 Geonics EM61 MkII**

The EM61 MkII is a pulsed-induction sensor which transmits a short electromagnetic pulse (a unipolar rectangular current pulse with a 25% duty cycle) into the Earth. The instrument consists of two air-core 1m x 0.5m coils housed in fiberglass, a backpack containing a battery and processing electronics, and an optional data logging device. The lower coil serves as the transmitter and main receiver. The upper (receiver only) coil lies 30cm above the bottom coil. Metallic objects interact with this transmitted field which induces secondary fields in the object. These secondary fields are detected by the receiver coils that are collocated with and above the transmit coil. An example EM61 MkII sensor mounted on a test platform is shown in Figure 2-1.



Figure 2-1 – Geonics EM61 MkII coils on a test platform

The transmitter pulse repetition rate is 75 Hz, corresponding to a base period of 13.333 milliseconds. The transmit pulse is 3.333 milliseconds long with a linear ramp off on the order of 100  $\mu$ s. The EM61 MkII electronics can be operated in one of two modes: 1) in 4-channel (“4”) mode with 4 time “gates” (216, 366, 660, and 1266  $\mu$ sec) for the bottom receiver coil or 2) in Differential mode, in which 3 time “gates” are measured from the bottom coil (216, 366, 660  $\mu$ sec), and one is measured from the top coil (at 660  $\mu$ sec). The transient decay voltage profile is sampled in the four time windows (for one or two receiver coils, as is appropriate) and analog integrated. The analog-integrated voltages are then sampled by the instrument’s analog-to-digital (A/D) converter. The analog integration step has a dynamic time response that both shifts and modifies the sensor’s response. The sensor’s step response is given by the manufacturer as:

$$e(t) = 1 - \frac{1}{\sqrt{1 - \tau^2}} \exp(-\tau\Omega t) \sin(\Omega t \sqrt{1 - \tau^2} + \arccos(\tau)),$$

where  $\Omega = 7.5$  rad/sec and  $\tau = 0.9$ .

The output of the pulsed-induction sensor can be sampled at rates up to 15 Hz, resulting in a data station spacing of approximately 10 cm at normal walking speeds. The analog integrated voltage is sampled each time the electronics receives a trigger event. The trigger can either be a hardware pulse or a trigger character sent via RS-232 from the data acquisition software. Each trigger event results in a binary data packet being sent via RS-232 to the data acquisition software. The details of the binary data packet format are given in the EM61 MkII documentation [2].

One important factor to note is that the transmit current changes in amplitude as the system battery discharges. The measured output voltages should be corrected for this changing current. The nominal transmit current for a standard EM61 MkII will be reported as a value of 3,000 and 1,800 for the –HH variant. The reported current is then used to normalize the voltage outputs to measurements made at the reference transmit current. Both the measured channel output voltages and the measured current are therefore potential sources of noise and error in the final sensor output.

Data are recorded using the vendor-provided Juniper Systems Allegro handheld data logger. For this demonstration, the EM61 MkII was operated in Differential mode and data were collected at 10 Hz using a custom software package written at NRL on a laptop computer. The facility for recording fiducials or ‘marks’ during the data collection process is provided for the purposes of co-registration data sets as necessary.

### 2.1.1.2 Geonics EM63

The EM63, shown in Figure 2-2, operates using the same principles as the EM61 MkII, with two major differences, the coil geometry and the number of time gates recorded. The transmitter coil for the EM63 is 1m by 1m in dimension, normally operated at a height of approximately 40cm above the ground surface (wheel mode). The three receiver coils measure 0.5m x 0.5m, with the lowest mounted at the same height as the transmitter coil, and two other coils of the same size mounted at 30cm and 60cm above the lowest coil. Rather than recording a maximum of 4 time gates, the EM63 records data from 26 geometrically spaced time gates, from 180 $\mu$ s to 25ms.

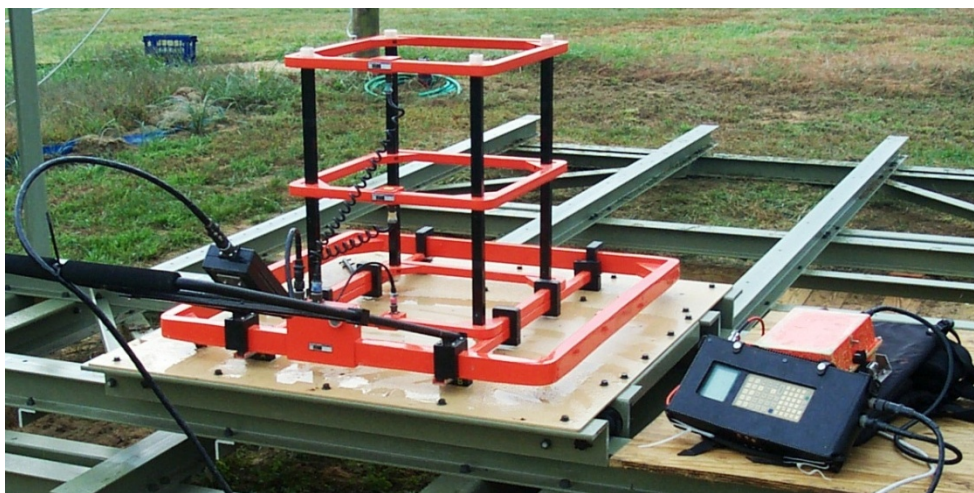


Figure 2-2 – Geonics EM63 with electronics and data logger, on a test platform

Data were collected using the integrated data logger field PC provided by Geonics at approximately 4 Hz and periodically downloaded for analysis.

### 2.1.1.3 Geophex GEM-3

The GEM-3 sensor (Geophex, Ltd.) is a frequency domain electromagnetic instrument, utilizing concentric coils mounted in a fiberglass sensor head. The sensor head is a disk, available in three sizes ranging from 40cm to 1m in diameter. The 40 cm sensor used in this demonstration is shown in Figure 2-3. This sensor’s coil head consists of a 40 cm diameter transmit coil with 12 turns, a 23 cm diameter bucking coil with 6 turns, and a 12 cm diameter receive coil with 100 turns. The counter-wound (with respect to the transmitter coil) bucking coil establishes a “magnetic cavity” around the receiver coil. To measure the strength of the transmit field, a reference coil (3 cm in diameter with 22 turns) is positioned between the transmit and the bucking coils. The transmit current depends on the set of frequencies used and the battery’s charge state; therefore the reference coil measures the transmit field strength directly and is used

to convert the received signal in the relative units of parts-per-million (PPM) with respect to the transmitter.

The sensor transmits a composite waveform of up to 10 separate frequencies in a range of 30 Hz to 96 kHz. The sensor's base period is  $1/30^{\text{th}}$  of a second. All transmit frequencies have an integer number of periods within this base period. The sensor's A/D measures the receive coil and reference coil responses over the base period (6400 samples over  $1/30^{\text{th}}$  second). The receive coil output is convolved over one base period with the reference coil to calculate the in-phase and quadrature responses at the transmit frequencies in relative PPM units. This gives a maximum data rate of 30 samples per second. There are software options for averaging over a specified number of base periods. Most of the data presented in this report were averaged over three base periods for a data rate of 10 samples per second. For this demonstration, ten frequencies with roughly logarithmic spacing were collected (90, 150, 270, 570, 1230, 2610, 5430, 11430, 20010, 44370 Hz). For some measurements a broader frequency range was explored (30, 90, 150, 450, 1170, 3930, 13590, 39030, 59010, and 90030 Hz). Data are wirelessly transmitted (via Bluetooth technology) from the GEM-3 electronics to the vendor-provided iPAQ. The internal battery was removed and a connector added for the use of external battery packs to extend measurement times.

Measurements of a ferrite rod are used to correct the phase-shifted GEM-3 output and the built-in correction factors appear to be good to within a fraction of a percent. The system is capable of collecting the entire A/D output over one base period and save it to a data file. This can be done in both passive (no transmit current) and active (transmit on at configured set of frequencies) modes. This feature was used to assess the effect of external noise on the GEM-3. The facility for recording fiducials, or 'marks,' during the data collection process is also provided in addition to the notion of survey line numbers for the purposes of data registration.



Figure 2-3 – Geophex GEM-3 sensor head (40cm diameter) and electronics

#### **2.1.1.4 Position and Orientation**

Position information was recorded using a real time kinematic (RTK) GPS system, updated at a rate of 10 Hz. GPS positions are expected to be accurate within  $\sim$  (1-2 cm H, 2-3 cm V) under optimal conditions. The GPS data were recorded using a custom logging software package written at NRL and a laptop computer. All navigation and sensor data are time-stamped with Universal Coordinated Time (UTC) derived from the satellite clocks and recorded by the data acquisition computer. The facility for recording fiducials or ‘marks’ during the data collection process is provided for the purposes of data co-registration. Some testing conducted during this demonstration did not require the position of the instrument to be recorded, such as the static sensor noise testing. An inertial measurement unit (IMU, Crossbow VG300) was used to collect platform orientation (e.g. roll angle) information at update rates of up to 110 Hz. The same logging software is used to collect and timestamp the data. A higher-bandwidth IMU (Crossbow IMU 400) was used for the additional data collection conducted during the data analysis phase of this demonstration.

#### **2.1.2 NRL Low Frequency Spectrum Analyzer**

Sources of external noise of interest to this study included those within the sensor bandwidth such as power lines and those of sufficient power that leakage into the sensor bandwidth is significant such as radar transmitters at airports. Each sensor design has a unique sensitivity to external noise based on factors such as detection bandwidth, pre-filtering, etc. Independent measurement of the external EM radiation impinging on the EMI sensors was made using a custom-build low-frequency spectrum analyzer based on a 0.5 m x 1.0 m EM61 receive coil (top). A custom-build solution was required because commercially-available spectrum analyzers do not have the capability of operating at the low frequencies required to match the operational window of the geophysical sensors being evaluated (DC – 100 kHz nominal).

The output terminals of the receive coil were directly connected to an analog input of a data acquisition card (National Instruments, DAQCard 6036E, 200 kS/sec). A custom data acquisition software package was developed to acquire data over a user-selectable frequency range (0.5 Hz – 100 kHz max). High resolution within the frequency range (0.19 Hz) is provided with a good dynamic range (75 – 100 dB). Data are recorded as a voltage time series. The prototype shown in Figure 2-4 is reasonably rugged. The cable breakout box (shown under the laptop) used is a generic one which could easily be further ruggedized and miniaturized by simply placing the breakout panel in a custom enclosure.

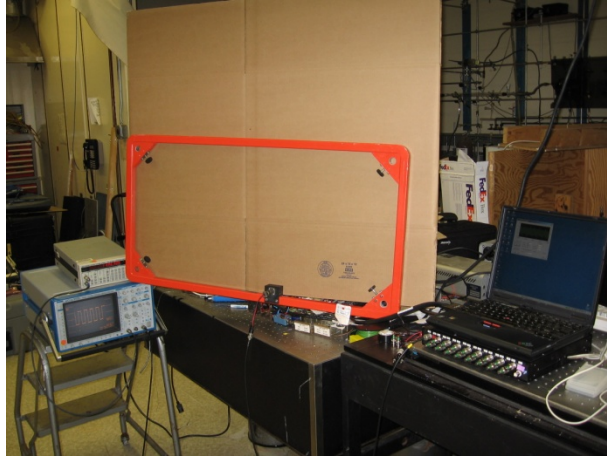


Figure 2-4 – NRL Low-Frequency Spectrum Analyzer

### 2.1.3 Test Platforms

Testing was conducted using three different platforms to carry the sensors. The platforms tested were a man-portable cart, a specially constructed test tower, and the NRL MTADS EM trailer. These platforms are pictured in Figure 2-5, Figure 2-6, and Figure 2-7.



Figure 2-5 – Man-portable cart



Figure 2-6 – Rail system and test tower



Figure 2-7 – MTADS EM trailer

## 2.2 Advantages and Limitations of the Technology

Ultimately, the advantage of understanding the magnitudes and sources of noise for EMI sensor, the components of the error budget, and using this knowledge will be the ability to characterize a site quickly and identify what technologies can be successfully implemented for the detection and discrimination of UXO. A successful choice should lead to a reduction in the number of false positives, and therefore the costs of remediation in UXO contaminated areas. By conducting these demonstrations in a variety of environments, one could obtain information applicable to UXO sites in similar terrains and noise environments across the continental United States.

### 3. Demonstration Site

#### 3.1 Test Site Selection

All data for this project were collected at Army Research Laboratory's Blossom Point Research Facility, the home of NRL's MTADS program. It provides the obvious benefit of being where NRL's equipment, tools, offices, etc. are located so that we could efficiently develop our procedures and standards for testing. Beyond that, however, it provides many of the features we would look for in a "typical" survey site in the Eastern United States. A variety of areas are available ranging from open field areas, heavily treed sites, to transition zones. One might expect the geologic interference to be at a minimum at a site such as this but we have shown in previous testing for other programs that there is a surprising amount of short-scale geologic variation present even at Blossom Point. In this, it is analogous to what we have observed at the Standardized UXO Test Site at Aberdeen Proving Ground, another prototypical Eastern site. Finally, the Blossom Point Site is an active test range and is adjacent to the NRL Tracking Station which houses a number of communications facilities, providing a meaningful measurement of external noise.

##### 3.1.1 Test Site History / Characteristics

The Army Research Laboratory's Blossom Point Research Facility is comprised of 1,600 acres, approximately 50 miles south of Washington DC, in rural Charles County, Maryland, Figure 3-1. The facility is located on Cedar Point Neck, between the Nanjemoy Creek and the Port Tobacco River on the northern shore of the Potomac River. Open, grassy fields, as well as areas of deciduous and mixed deciduous and conifer forest are found on the property. Low elevation, swampy areas are present in the central and eastern portions of the property, and along the southern edge, adjacent to the Potomac River, Figure 3-2.

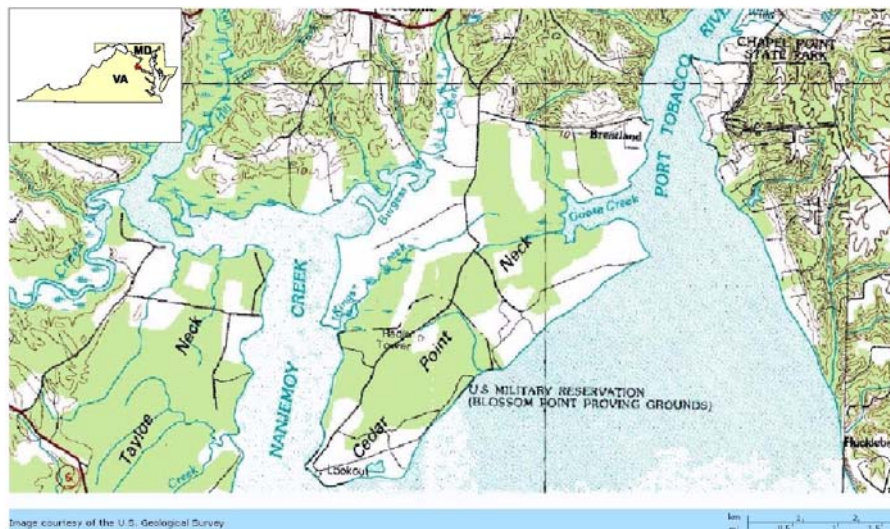


Figure 3-1 – Location of Army Research Laboratory Blossom Point Facility

### 3.1.2 Climate

Blossom Point has a climate typical of the Mid-Atlantic States, with moderately cold, damp winters and hot, humid summers.

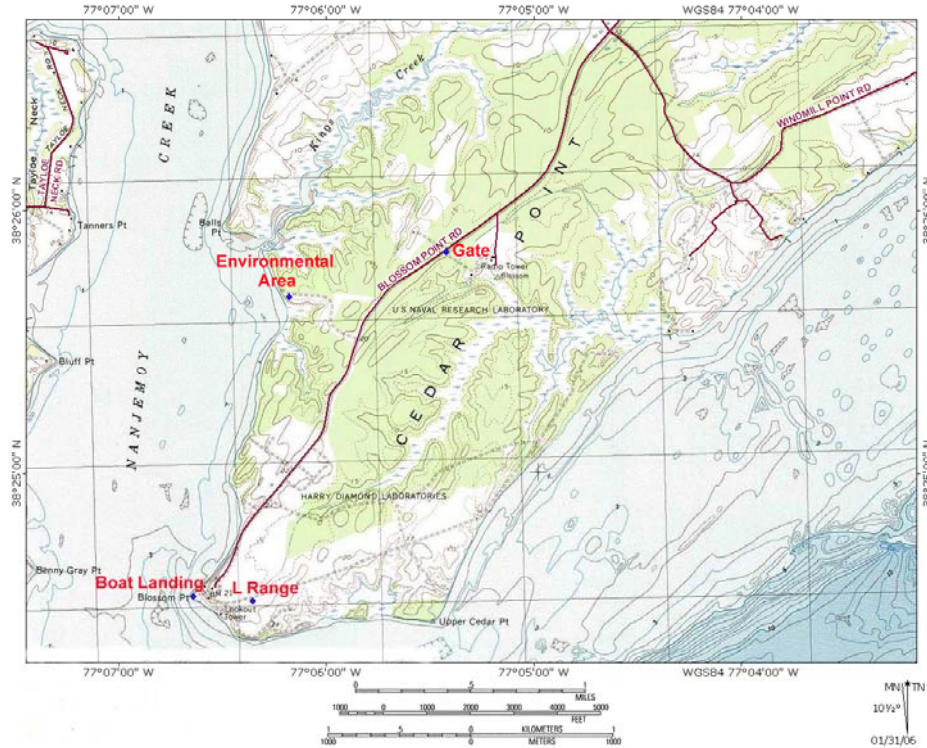


Figure 3-2 – Topographic Map of Blossom Point Research Facility, showing locations of selected EMI Noise test sites

### 3.1.3 Geology

Charles County, MD is situated within the Coastal Plain Province. This province is underlain by an eastward thickening wedge of unconsolidated marine sediments including gravel, sand, silt, and clay. The Maryland Point Formation is described as fine to coarse grained sand, well to poorly sorted in the upper third, with poorly sorted silty clay in the lower part, with a pebbly sand at the base. [3]

Two other mapped units occur on Cedar Point Neck, each occupying small areas. The Upper Pleistocene-aged Kent Island Formation occurs only on a peninsula south of Goose Creek. This unit overlies the Maryland Point Formation, and consists of fine to medium grained, moderate to poorly sorted silty sand. Minor silty to sandy clay is also present. The most recent mapped unit is Holocene deposits, undivided, which occur only in low lying areas adjacent to swamps and drainages at the Blossom Point Research Facility. These deposits include poorly sorted sand and gravel, as well as well sorted sand, silt and clay. The maximum thickness of the Maryland Point Formation on Cedar Point Neck is approximately 40 feet. The formation is absent where the cross section traverses two small streams, filled with Holocene sediments.

Geologic responses observed in electromagnetic surveys are often caused by magnetic minerals, primarily magnetite and maghemite. These minerals are very likely present in the marine sediments at Blossom Point, though it is expected that they are generally dispersed, and that concentrations high enough to affect EM response are limited in area.

### **3.1.4 Test Locations within Blossom Point**

Three selected locations at Blossom Point were used to replicate conditions typical of live UXO sites located in the Eastern US, the Boat Launch, the Environmental Area, and a selected portion of the L-Range, Figure 3-2. At each of the sites, described below, a series of measurements were made as described in Section 4 including data collection with the EMI instruments at various heights, the use of the rails system / test tower, traverses with various sensor combinations, and standard geophysical measurements of the soil properties.

#### **3.1.4.1 Environmental Area**

A transitional area leading into dense woods with a thick foliage cover was used as one test site at Blossom Point and is shown in Figure 3-3. The encroaching tree line did cause degradation of the GPS fix quality which proved useful for examining the effects of GPS satellite constellation geometry.



Figure 3-3 – Environmental Area, view to the East

#### **3.1.4.2 Boat Launch**

The Boat Launch Area was a test location at the southern tip of the Blossom Point facility with a low elevation and corresponding saturated soils. The location is also known as the former Munitions Storage Area. This area was selected for this demonstration and is shown in Figure 3-4. The effects of the wetter soils were compared to unsaturated sediments in the other test

locations. This site offered open, unobstructed sky view, for ideal GPS satellite reception. Due to the low elevation, the Boat Launch site experienced the most variation on soil moisture during the course of the demonstration.



Figure 3-4 – Boat Landing Area, view to the southwest

### **3.1.4.3 L Range**

A site was selected on the L Range, an active range, in an area which generally did not interfere with the ongoing usage of the range. The site, shown in Figure 3-5, exhibited a background typical for a former firing range, with buried ordnance and ordnance scrap underlying the survey area. The surface had been cleared of any munitions or debris, and the vegetation (grass) was mowed prior to our data collection.



Figure 3-5 – Active Range Test Location, L-Range, view to the East

## 4. Noise Source Analyses

### 4.1 Inherent Noise of Geophysical Sensors

Any actual EMI sensor contains a certain level of inherent noise. This noise is manifest as the response values reported by an instrument that cannot be accounted for by any outside source. Difficult to remove through post-processing techniques, inherent noise must be expected and accounted for during all EMI surveys. The results of these measurements, while only valuable to the sensor design community as a benchmark against which to measure their development efforts, can be expected to be very valuable to those developing classification algorithms and systems.

To measure the basic electronic noise levels of the GEM-3, the sensor was placed stationary on a test stand, in a field far removed from any radiating object. After warming the sensor up for 15 to 30 minutes, data were collected for another 30 minutes. The GEM-3 was run with ten transmit frequencies from 30 to 90,030 Hz. The sensor was set to average over three base periods; so, data were collected at ten samples per second. A time raster at 3930 Hz and the associated, averaged power spectra are plotted in Figure 4-1 and Figure 4-2. In-phase is shown in black and quadrature in red. At each transmit frequency, there is a basic white noise level for both in-phase and quadrature. The white spectra roll off above 1-2 Hz because of the base period averaging. On time scales greater than 10 seconds, there is significant drift in the in-phase signal. This is possibly due to changing conditions in the imperfectly bucked primary field. At high frequencies, this drift is present in the quadrature signal as well. Figure 4-3 plots the white noise floor as a function of transmit frequency. From these results, the optimal transmit range for the GEM-3 is from 1 to 10 kHz.

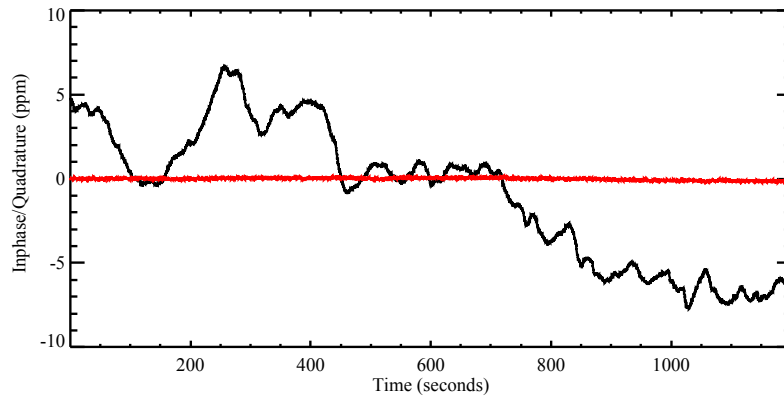


Figure 4-1 – A time raster plot of the in-phase and quadrature static response of the GEM-3 at 3,930 Hz. The in-phase and quadrature responses are shown in black and red, respectively.

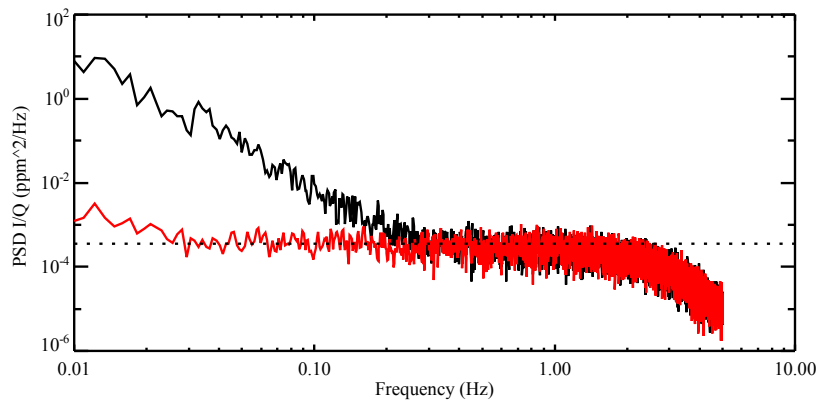


Figure 4-2 – Averaged power spectrum of the in-phase and quadrature static response of the GEM-3 at 3,930 Hz. The in-phase and quadrature responses are shown in black and red, respectively. The white noise floor is shown as a dashed line.

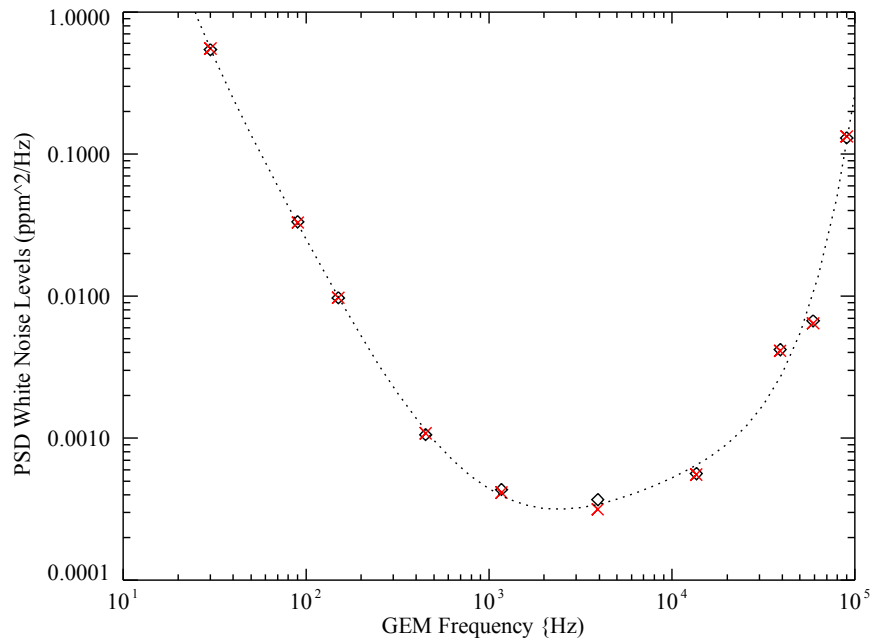


Figure 4-3 – White Noise Levels for GEM-3 Static Measurements. Measurements at each transmit frequency are shown as symbols (black diamonds – in-phase, red x’s – quadrature). A polynomial fit to the data is shown as a dashed line.

When placed in open fields away from power lines, the EM61 MkII measures very consistent low-level noise, consistent with the source being the sensor electronics themselves. EM61 MkII data were collected with the sensor operating in Differential mode and using the NRL logging software at a rate of 10 samples per second. In Differential mode, the first three data channels sample time windows increasingly later in time for the receive coil. The fourth data channel samples the top coil at the last time window from the bottom coil. The data were normalized by the measured transmit current and multiplied by the standard gain factors to give units of “milliVolts”. Data were collected for over one hour with the sensor remaining stationary. Figure 4-5 plots averaged power spectra for each data channel. As was seen with the GEM-3, each data channel has a basic white noise level between frequencies of 0.1 to 10 Hz. At lower frequencies (longer time scales), the sensor output begins to exhibit drift. Above 1 Hz, the spectra roll off as determined by the appropriate time response. The red curves plot the power spectral response as determined by the sensor’s step response equation discussed in Section 2.1.1.1. The dotted line indicates the digitizer signal floor (bit level) of the sensor’s A/D electronics. The noise observed for the later time gates is not significantly above A/D digitizer signal floor. For the particular data sequence shown in Figure 4-5, there were unexpected peaks at several frequencies. These peaks were not always present and their cause is currently unknown. The by-channel noise levels for the EM61 MkII are tabulated in Table 4-1.

Table 4-1 – Nominal EM61 MkII RMS Noise Characteristics and Digitizer Bit Levels

Channel	RMS Noise (mV)	Bit Level (mV)
#1	0.136	0.0872
#2	0.0911	0.0872
#3	0.0665	0.0872
#4 – Top	0.133	0.194

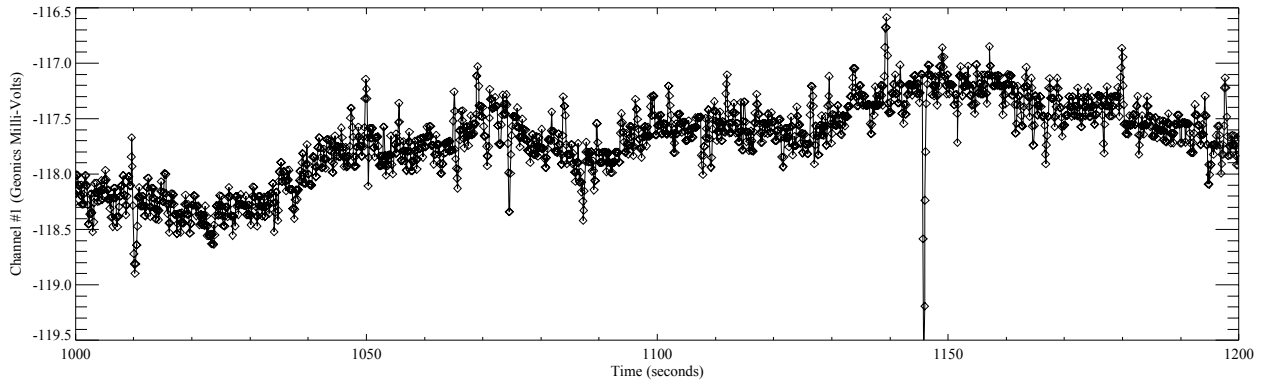


Figure 4-4 – Time Raster for time gate #1 of a Stationary EM61 MkII in a Quiet Location.

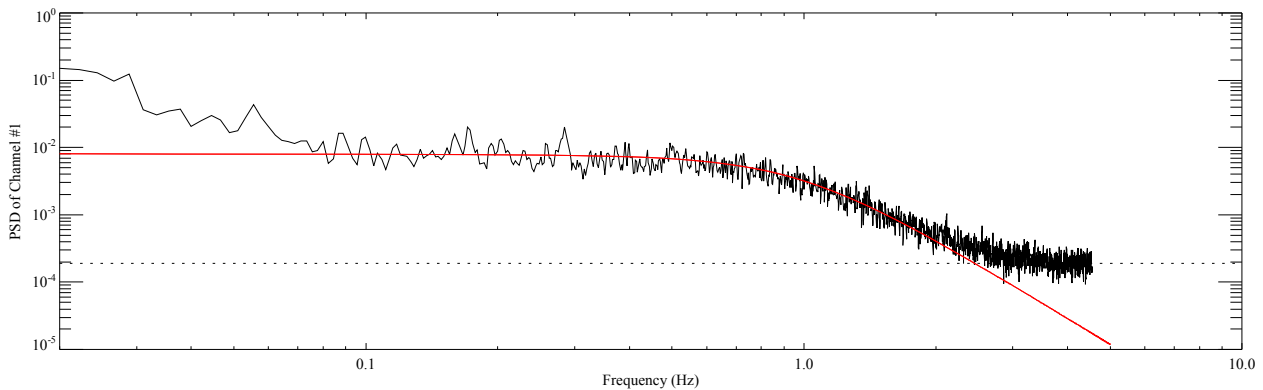


Figure 4-5 – Averaged Relative Power Spectra for a Stationary EM61 MkII in a Quiet Location. The dotted lines represent the channel-specific noise floor (bit level). The red curves plot the power spectral response as determined by the sensor’s step response.

## 4.2 External Noise Sources

External noise results from the presence of ambient EM signals that are detectable by the sensor. Typical sources include those within the sensor bandwidth such as power lines and those of sufficient power that leakage into the sensor bandwidth is significant such as with radar transmitters at airports. External noise has also been observed as a results of GPS equipment, data loggers, and batteries that are placed too close to the sensor during data collection. Each sensor design has a unique sensitivity to external noise based on factors such as detection bandwidth, pre-filtering, etc.

There are various sources of external noise which were found have measurable effect on the EM61 MkII sensor. These include: 60 Hz AC power distribution and harmonics, VLF/LF radio transmissions (1 to 10's of kHz range), and nearby electronics (50-100 kHz range). The GEM-3 shows similar spectral content when operated in a passive mode, with the transmitter off. For the GEM-3, leakage of the transmit field through the bucking field is a larger contribution than the external noise.

To assess the external noise picked up by the GEM-3's receiver coil, data were collected with the GEM-3 sensor in its monitoring mode. This mode dumps out the receive coil voltage measured by the A/D system over one 1/30<sup>th</sup> of a second base period (6,400 samples collected at 192,000 samples per second). When in passive mode, the transmitter is turned off; and when in active mode, the transmitter is turned on. These data were collected with the GEM-3 roughly 2 meters above the ground. Data were taken with the GEM-3 coil in three orthogonal orientations: horizontal, on edge facing north-south, and on edge facing east-west. In each orientation, data were collected while passive, while active with 10 transmit frequencies, and while active with three transmit frequencies.

Relative power spectra from two GEM-3 data sets are shown in Figure 4-6. The graph in black is the results from data collected in the passive mode. It clearly shows 60 Hz and a number of harmonics dominating the output. After this, there are some broad spectral peaks in the 10 to 100 kHz region. When the coil was oriented on edge, it picked up VLF transmission lines at 24 and 24.8 kHz. An 'active mode' spectrum with ten transmit frequencies is shown in red. The spectrum is dominated by the transmit frequencies. While the receive coil is located in a magnetic cavity created by the bucking coil, the primary field is not completely canceled. These peaks plus the general active background are much greater in amplitude than the passive spectra; only the lower 60 Hz harmonics appear to rival the active noise. Based on these results, external noise is not a dominant factor for the GEM-3 sensor.

Figure 4-7 plots the power spectra measured with the NRL low frequency spectrum analyzer discussed in Section 2.1.2 for oriented vertically, facing north at the Boat Launch Area. As with the passive GEM-3 measurements, 60 Hz and harmonics are present. There are also the VLF transmissions in the 20 kHz range. Unlike the GEM-3, there are a variety of lines from 100's of Hz out to kHz. In particular, a large consistent line is present at 2 kHz. There is a broad feature around 50 kHz. The amplitude of these features is comparable to the 60 Hz and VLF features.

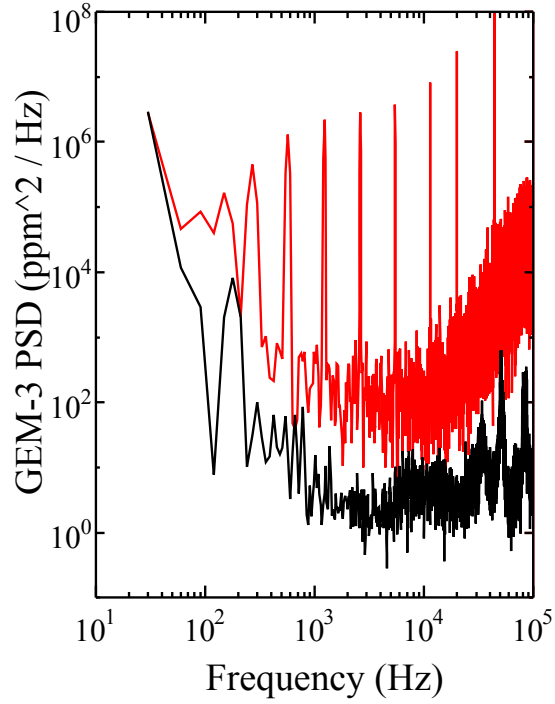


Figure 4-6 – Power Spectra Results for the GEM-3 Sensor in both Passive (black) and Active (red) Monitoring Modes

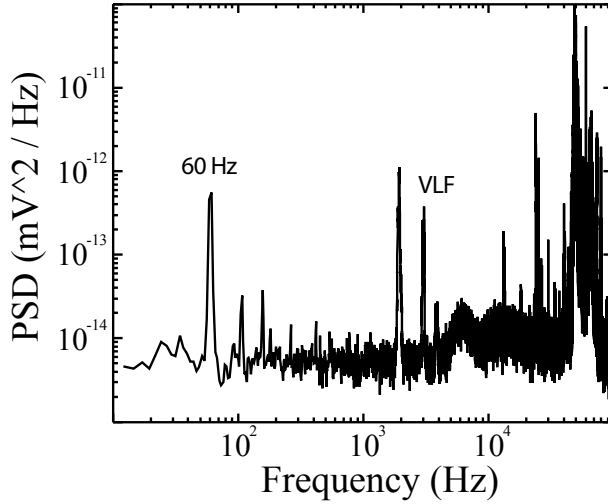


Figure 4-7 – External Noise Relative Power Spectrum for vertically oriented EM61 receiver coil facing north at the Boat Launch Area

### 4.3 Motion-Induced Noise

The role of motion-induced noise in the degradation of UXO classification ability has been well documented by us and others [4]. The two facets of what is commonly understood as motion-induced noise are noise resulting from motion of the receiver coil of the sensor in the Earth's field [5] and the variation in the observed signal resulting from orientation changes of the sensor as it bounces and twists over rough ground.

Consider an EMI sensor receiver coil moving in the Earth's field, as shown in Figure 4-8.

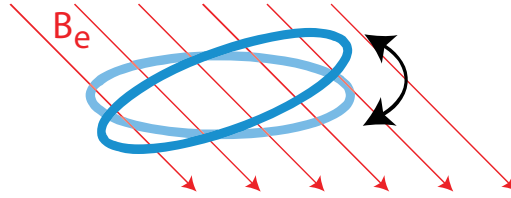


Figure 4-8 – Schematic drawing of an EMI sensor receive coil moving in the Earth's field.

The induced voltage in an EMI sensor receive coil with N turns can be calculated using:

$$V(t) = -N \int_A \vec{B}_E^e \cdot \frac{d}{dt} \hat{n}^e(t) da ,$$

where  $\vec{B}_E^e$  is the earth's field and  $\hat{n}^e$  is the normal unit vector of the coil, both in the earth reference frame. Assuming a uniform field across the coil, this can be written out in terms of orientation angles (roll- $\psi$ , pitch- $\theta$ , yaw- $\phi$ ), angular rates ( $\omega_x$ ,  $\omega_y$ ,  $\omega_z$ ), and the components of the earth's field. For the simplified case of a coil pitching in the north-south direction, this can be written as:

$$V(t) = NA\omega_y [B_y \cos(\theta) - B_z \sin(\theta)] ,$$

where north is along the y axis, ( $B_y$ ,  $B_z$ ) are the Cartesian components of the earth's field,  $\theta$  is the pitch angle, and  $\omega_y$  is the pitch rate. In general, the expression involves all three B components, all three angles and the roll/pitch rates.

Each EMI sensor processes these voltages differently. The EM61 MkII samples and integrates the decay response at four windows in time, or time gates. The GEM-3 convolves the  $\sin()$  and  $\cos()$  functions of the transmitter frequency of the data acquisition base period (33.3 msec).

Three different platforms were used to characterize motion-related EMI noise: the man-portable cart, a specially constructed rail/tower system, and the MTADS EM towed trailer platform (Figure 2-5, Figure 2-6, Figure 2-7 respectively). The first two were chosen as typical survey systems and the third was meant to contrast as an example of very smooth motion. Besides the GEM-3, each system had a GPS antenna attached to a tripod and an IMU bolted down in order to measure to nature of the platform's motion. At each of the three sites, these systems were moved back and forth along approximately the same track.

As one example, the GEM-3 was placed high on a test stand and moved in a controlled fashion. The sensor was placed at the end of a long board that could be pivoted off the edge of the test stand. The board was aligned along magnetic north. A second IMU (Crossbow IMU-400) with a higher data rate (130 Hz) and a wider bandwidth (3dB roll-off at 30 Hz for angular rates) was attached to the board. The GEM-3 was set to collect data at 30 Hz. With both GEM-3 and IMU running, data were collected with the board stationary, pitching slowly, faster, and fastest. Figure 4-9 presents the IMU measured angular pitch rate,  $\omega_y$ , the in-phase response at 90 Hz and the quadrature response at 90 Hz. At the slow pitch rate, there was no measurable GEM-3 response. The response increased with pitch rate.

From the IMU measurements, it should be possible to calculate the expected GEM-3 response. The voltage induced in the receive coil as a function of time equals the time rate of change of the magnetic field going through the receive coil. Given this voltage as a function of time, one can divide it into  $1/30^{\text{th}}$  of a second base periods and convolve it with the sine and cosine of the GEM-3 transmit frequencies. With a rough idea of the GEM-3 A/D conversion of volts into ppm, the actual GEM-3 response can be predicted from the IMU measurements.

Given  $V(t)$ , the GEM-3 response for transmit frequency  $\omega$  is given by convolving it with  $\sin(\omega t)$  for in-phase and  $\cos(\omega t)$  for quadrature over the GEM-3 base period of  $1/30^{\text{th}}$  of a second. For this short time scale, the induced voltage is to first order a linear function over the base period. The result is the integration of  $t \times \sin(\omega t)$  or  $t \times \cos(\omega t)$  over an integral number of transmit periods. The first integration produces a non-zero solution and the second solution is zero. The result to first order should be a large amount of sensor noise in the in-phase and a small amount in quadrature. This was not observed; some part of the induced voltage noise always leaked into the other channel. The manufacturer indicates that all of the noise should be in the quadrature response. After making measurements to convert voltages into ppm and accounting for other aspects of the GEM-3, the mixture of motion noise could not be adequately accounted for. To match the measured GEM-3 response from simple pitching motion, the voltage integration required an arbitrary phase shift of the form  $V(t) \times \sin(\omega t + \varphi)$  or  $V(t) \times \cos(\omega t + \varphi)$  where  $\varphi$  is a fixed phase shift of the transmit wave form relative to the measured base period. For the pitching experiment, a shift on the order of  $\pi/5$  radians was needed. Given this extra phase shift, the IMU measured motion can be used to closely model the measured GEM-3 response. With the phase shift, the in-phase and quadrature measurements could be closely matched at low GEM-3 transmit frequencies. At higher frequencies, the noise continued to decrease as expected for the quadrature, but the in-phase noise leveled out. It is thought that this residual noise maybe associated with flexing in the sensor coil head. For rapid motion in the earth's field, the noise for in-phase and quadrature scale roughly to the negative two power with transmit frequency. At GEM frequencies of 1 kHz, this noise becomes negligible relative to the sensor's inherent noise. The in-phase noise levels appear to level off above 1 kHz.

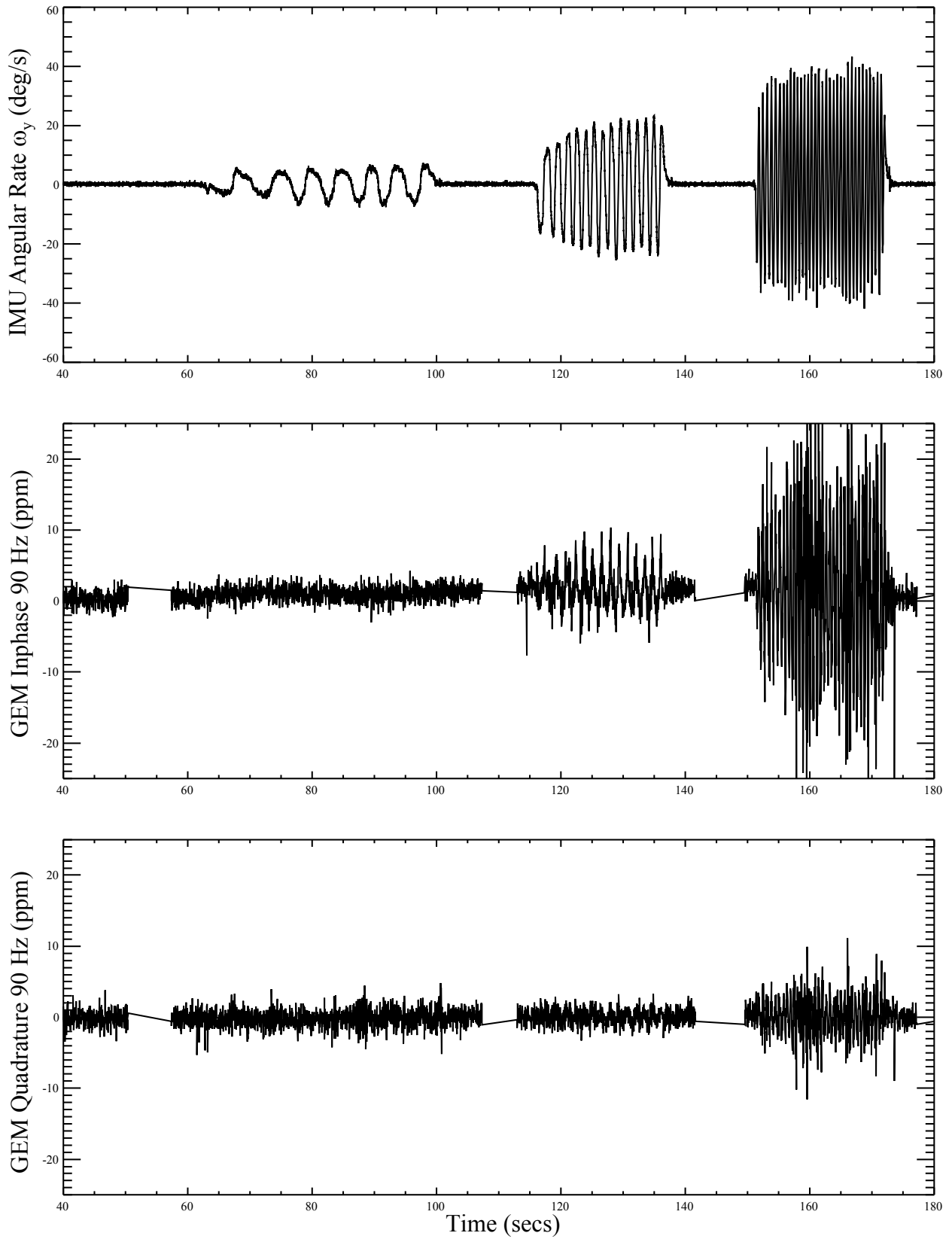


Figure 4-9 – IMU angular pitch rate versus the 90-Hz GEM-3 Response (In-phase and Quadrature)

As with the GEM-3, there are two dominant sources of motion-related noise for the EM61 MkII, voltages induced by the receiver coil moving in the earth's field and voltages induced by motion of the sensor relative to the ground. The same equations can be used to calculate the voltage induced in the EM61 MkII receive coils from the measured IMU roll, pitch, and angular rates. The voltage calculated from the motion measured by the IMU would then be time gated to the EM61's time gates and integrated using the sensor's dynamic response function. As long as this voltage changes on time scales greater than the sensor's pulse rate (75 Hz), all of the time gates will sample the exact same noise. Because of the sensor's response function, the measured voltage will be shifted in time. At higher frequencies, the measured voltage will also be reduced in amplitude.

Figure 4-10 plots fifteen seconds of data as the EM61 MkII was pitched at a rate of once every two seconds. The top graph shows the measured angular pitch rate. The bottom graph shows the measured EM61 MkII data channels shifted slightly for comparison. The EM61 MkII was operated in 4-channel Mode and the data from each time gate are shown in magenta, blue, red, and green, respectively by gate center delay. The black curve is the expected output based on the measured IMU motion. The induced voltage was calculated from the pitch rate and pitch angle as a function of time, filtered by the sensor's dynamic response, and multiplied by a fixed gain factor. Note that both the measured EM61 MkII response and the modeled signal are shifted from the pitch rate by approximately 0.4 seconds because of the sensor response function. Figure 4-11 plots the measured and modeled EM61 MkII signals as the frequency and amplitude of the pitch rate are increased. The red and green curves are the measured EM61 MkII third and fourth time gates; the black curve is the expected signal based on the IMU measured motion. The frequency of the pitch rates are roughly 0.22, 0.5, 1.0, and 2.0 Hz. The peak-to-peak amplitudes of the pitch rate range from 10 to 60 degrees per second. The induced EM61 MkII signal initially increases with increasing pitch rate, but from 1 to 2 Hz, the sensor's dynamic response begins to significantly damp the induced noise.

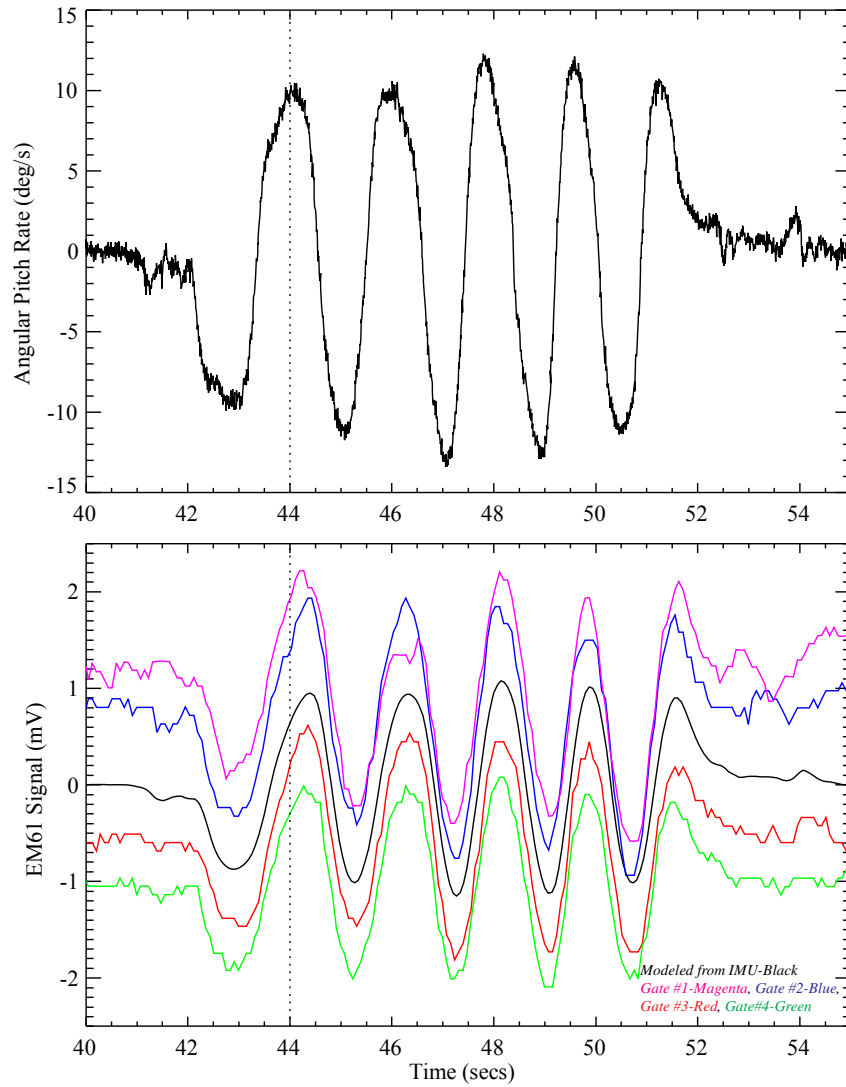


Figure 4-10 – Measured Response from an EM61 MkII while Undergoing Controlled Pitching. The top panel shows the sensor motion as measured by the IMU. The channel data are shown in the bottom panel as color-coded lines (time gates 1 – 4, magenta, blue, red, and green, respectively). The black line represents the modeled response using the IMU data.

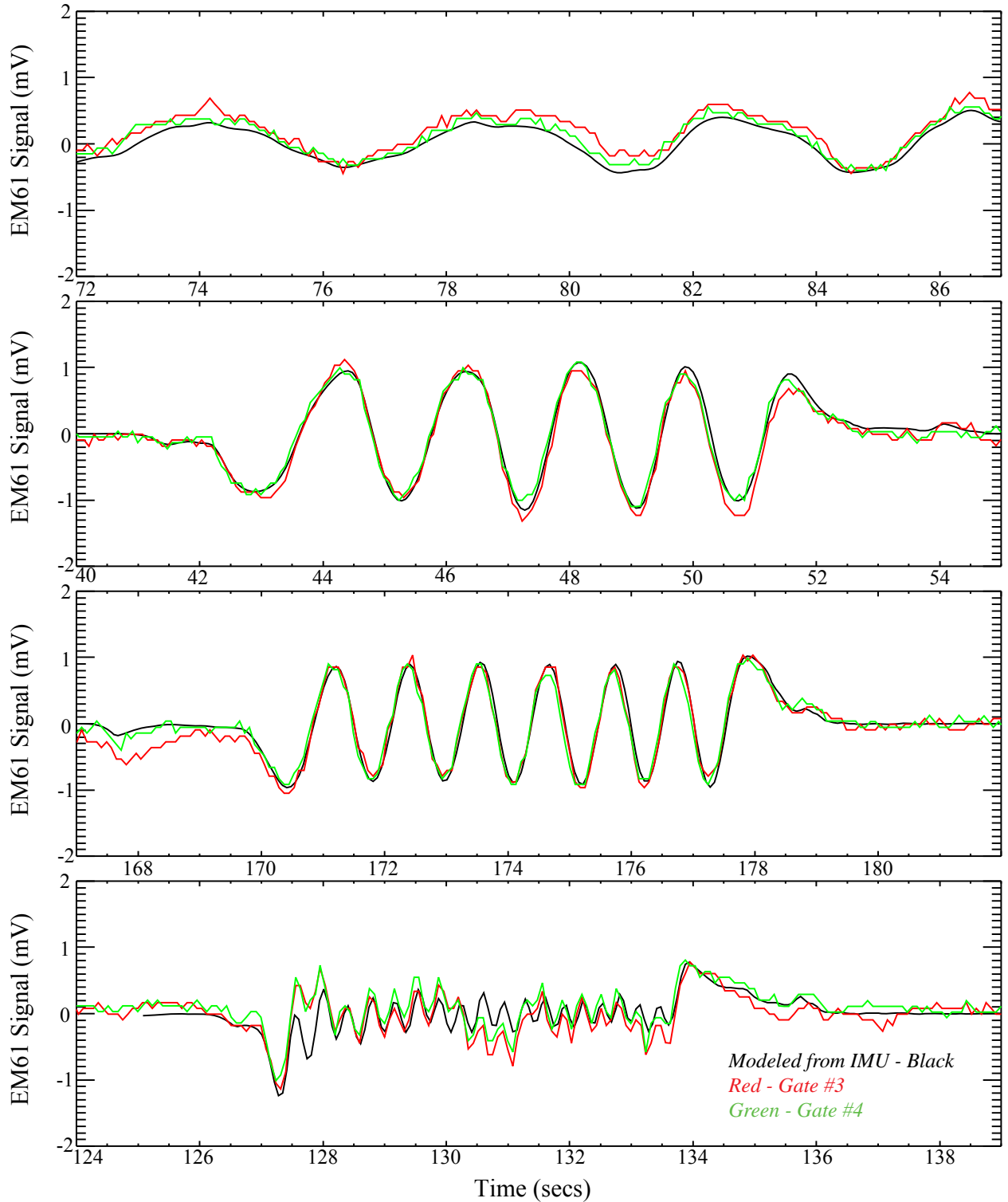


Figure 4-11 – Modeled and Measured EM61 MkII Response (for Various Pitching Rates. The channel data are shown as color-coded lines (time gates 3 – red and 4 - green). The black line represents the modeled response using the IMU data.

#### 4.4 Characterization of the Soil by Standard Techniques

At each location, the moisture content and magnetic susceptibility of the soil were measured using traditional geophysical techniques. Soil moisture content was measured at three stations within each test location. Magnetic susceptibility was measured by recording values at intervals, of approximately 0.75m for the Environmental and Boat Launch Areas and 1.0m for the L-Range Area, along the same path as the test rails.

##### 4.4.1 Soil Moisture

At each station, the soil moisture content was measured simultaneously at five depths (7.5, 22.5, 37.5, 60, and 90 cm). Soil moisture influences conductivity, which is expected to have a greater impact on frequency domain EMI instruments than on time domain instruments. Soil moisture was measured using a “Moisture Point” probe and electronics from Environmental Sensors Inc. (ESI). The results for representative measurements at the Boat Launch Area, Environmental Area, and the L-Range are shown in Figure 4-12. The variation between the locations was found to be larger than that between individual stations. To illustrate this, the results are presented in Figure 4-12 where an average value for each depth / location pair is shown with the range expressed as a horizontal error bar. As one might expect, the moisture content tracked with elevation above the river, with the highest content for the Boat Launch, lower at the L-Range, and a minimum at the Environmental Area. Interestingly, for depths of less than 40 cm, the moisture content was the same for all areas as shown in Figure 4-12.

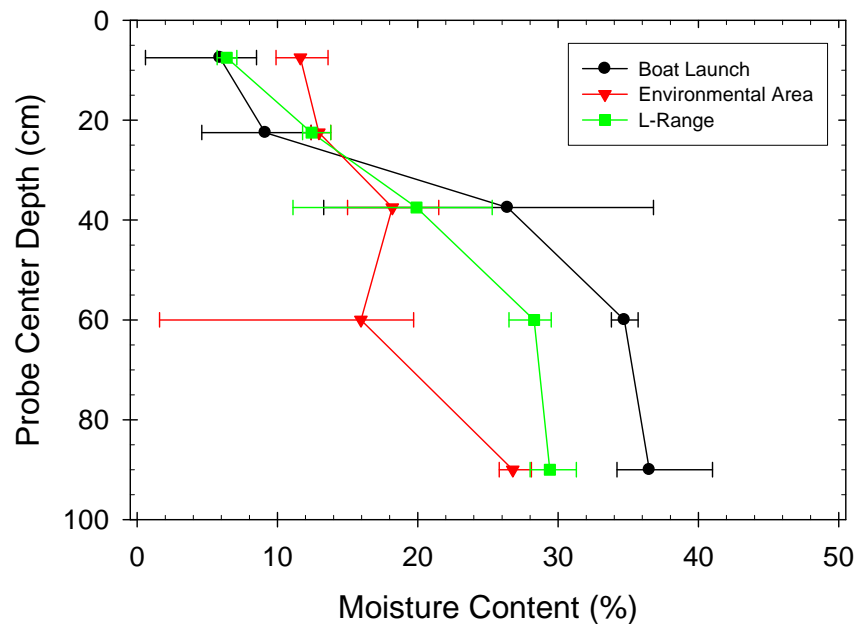


Figure 4-12 – Moisture content profiles for the Boat Launch, Environmental, and L-Range areas

#### 4.4.2 Magnetic susceptibility of soils

Magnetic minerals (especially magnetite and maghemite) in soil or shallow bedrock may have pronounced effects on EMI measurements. The Bartington MS2 Magnetic Susceptibility system is designed to measure soil magnetic susceptibility in the field. We used the Bartington MS2D search loop, 185mm in diameter, to measure differences in magnetic susceptibility of the soils underlying the traverse at each test location. Measurements were made at 0.75m intervals along the measurement traverse path for the Environmental and Boat Launch Areas. In the case of the L-Range measurements, measurements were made along two 92-meter long paths placed within a few meters of the rail system traverse at 1m intervals. The results are shown in Figure 4-13 and Figure 4-14.

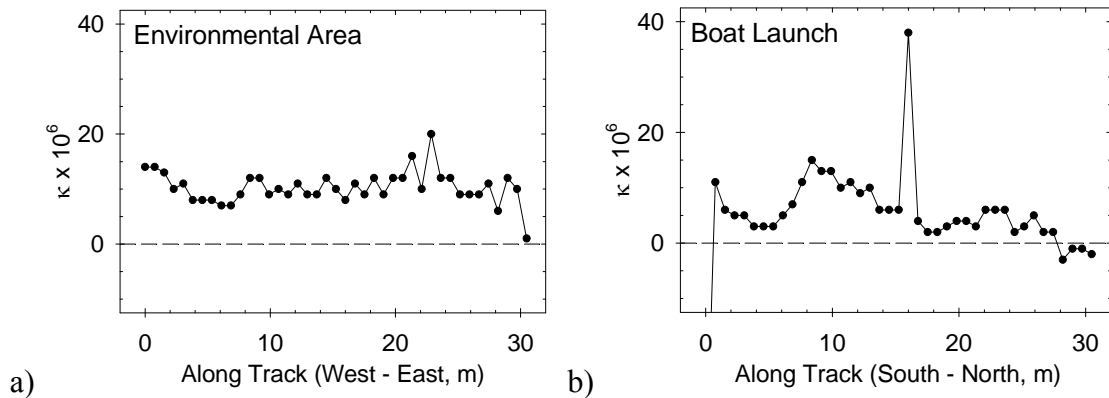


Figure 4-13 – Magnetic susceptibility profile for a) the Environmental Area, and b) the Boat Launch Area

In general the magnetic susceptibility of the soils at Blossom Point is quite low, on the order of  $5 \times 10^{-6} \kappa$  (cgs units). For reference, pure magnetite has a  $\kappa$  of 1 and the  $\kappa$  for solid iron can be on the order of 100 in the same units. The Bartington instrument exhibited a manufacturer-acknowledged drift rate that is particularly observable in Figure 4-14 due to the length of time involved in the measurement series (half an hour or so). The manufacturer provides enhanced data collection procedures (frequent, intermediate zeroing of instrument in air) and data-processing techniques for removing this drift.

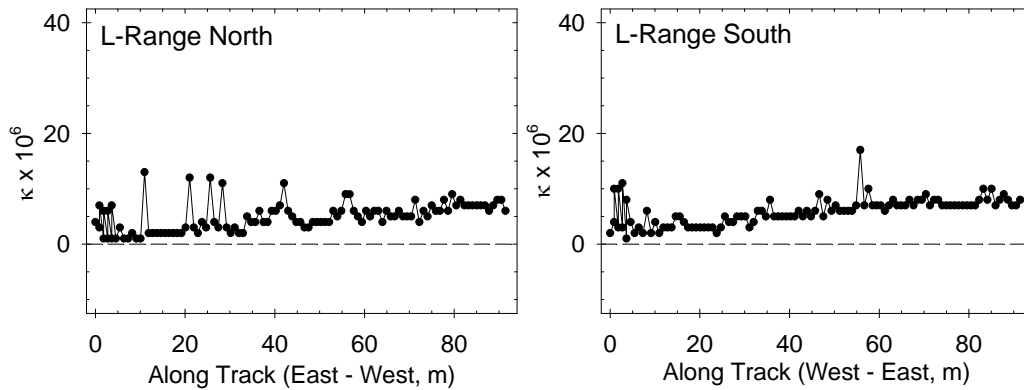


Figure 4-14 – Magnetic susceptibility profile for the L-Range traverses

## 4.5 Response to Ground

Non-metallic features in the subsurface have been documented as causing anomalous response in EMI instruments. While more correctly called background rather than noise as it is defined above, variations in this background response that occur on the scale length of UXO targets obscure the true target anomaly and complicate the classification decision. The geologic responses found in areas containing strongly ferromagnetic soils or bedrock have been well documented [6]. Fresh basaltic bedrock, like that found in Hawaii, appears to have the greatest impact on EM data, though similar responses have been observed in iron-rich soils in northern California.

The height above ground of an EMI sensor changes as the sensor moves across real-world terrain, as is shown schematically in Figure 4-15. The conductivity,  $\sigma$ , and the susceptibility,  $\chi_0$ , of the soil may both vary across the area being measured, even for small areas. For the GEM-3 sensor, the in-phase and quadrature ‘noise from soil,’ or response, have different, but distinctive, behaviors. For the EM61-MkII, a series of measurements at carefully-controlled heights were compared to available models. The susceptibility was shown to reproduce the  $t^{-1}$  response predicted for a step response. The EM61-MkII has 0.013 sec base period with a 25% duty cycle. The NRL TEMTADS sensor, an advanced EMI sensor, has a 0.05 sec base period with a 50% duty cycle. Measurements at carefully-controlled heights above the ground were consistent with a susceptibility of  $\sim 10^{-4}$ . The conductivity response followed a  $t^{-5/2}$  dependence. The conductivity was not measurable for the range  $\sigma \sim 0.002$  to 0.1 mho/m with these time-domain sensors. EM61 MkII sensors are sensitive to varying susceptibility,  $\chi_0$ . The ground-response noise observed by the EM61 MkII is correlated across, but decaying with the time gates.

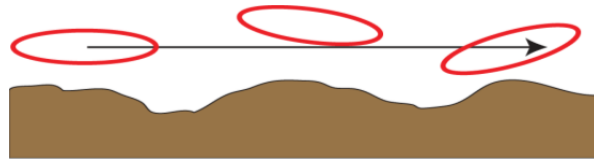


Figure 4-15 – Schematic drawing of an EMI sensor receiver coil moving across a ground surface.

The response of EMI sensors to soil has been investigated and modeled extensively in both geophysical and landmine situations [7-10]. The soil can be considered as a half space with both electrical conductivity,  $\sigma$ , and magnetic susceptibility,  $\chi$ . For a coaxial sensor with a circular transmit coil of radius  $a$  and circular receive coil of radius  $b$ , the voltage induced by a sinusoidal transmit field of frequency  $\omega$  can be expressed as:

$$v = i\mu_0\omega\pi ab \int_0^{\infty} \Gamma(\lambda, u_1, \chi) \times J_1(\lambda a) J_1(\lambda b) \exp(-2\lambda h) d\lambda,$$

where  $h$  is the height above ground,  $u_1 = \sqrt{\lambda^2 + i\sigma\mu_0\omega}$ , and:

$$\Gamma(\lambda, u_1, \chi) = \frac{\lambda(1 + \chi) - u_1}{\lambda(1 + \chi) + u_1}.$$

$J_1$  is a Bessel function of the first kind and of order 1.  $\lambda$  is the variable of integration. For the GEM-3 sensor, the voltage induced can be calculated by differencing the voltages induced for the transmit/receive and the bucking/receive radii combinations. To express the result in GEM-3 units of parts-per-million (ppm), one can calculate and divide by the voltage that would be induced directly in the receive coil by the transmit coil if the bucking coil were not there given by:

$$v = i\mu_0\omega\pi ab \int_0^\infty J_1(\lambda a)J_1(\lambda b)d\lambda.$$

The soil conductivity can be represented with a frequency independent real constant. In general, it has been found to be necessary to represent the soil magnetic susceptibility with a complex, frequency dependent term [7,11,12]. While various forms of this frequency dependence have been proposed, we have chosen to start out fitting GEM-3 measurements of the soil with a complex frequency-independent susceptibility of the form:  $\chi = \chi_R + i\chi_I$ . Numerical integration was used to evaluate these equations and sample results are shown in Figure 4-16.

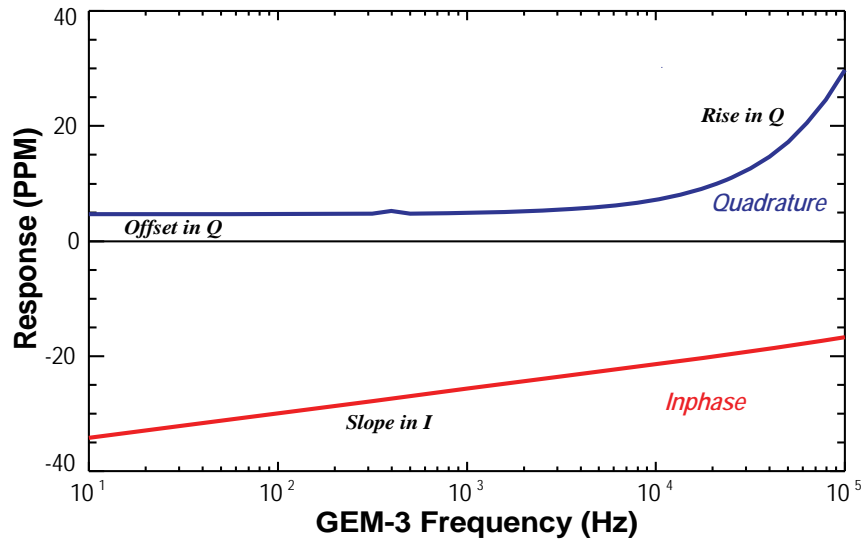


Figure 4-16 – Soil Model Response for the GEM-3 sensor. In-phase response is shown in red and quadrature response is shown in blue.

Figure 4-17 plots the results of the GEM-3 response based on this model. The sensor height input is 0.15 m. The solid curve soil parameters are: conductivity of 0.01 mho/m, real susceptibility of  $5.0 \times 10^{-4}$ , and imaginary susceptibility of  $-0.5 \times 10^{-4}$ . The dotted curve soil parameters are the same for susceptibility, but an increased conductivity of 0.1 mho/m. The black curves are in-phase and the red curves quadrature. The in-phase response (black curve) is negative and constant up to frequencies of 10 kHz. The amplitude of this response is driven by the magnitude of the real susceptibility term. As soil conductivity increases, the high frequency in-phase

response begins to curve towards zero. The quadrature response has a small positive offset at low frequencies that is a result of the small, negative, imaginary term for the susceptibility. At higher frequencies, the quadrature response increases and has larger values for higher soil conductivities.

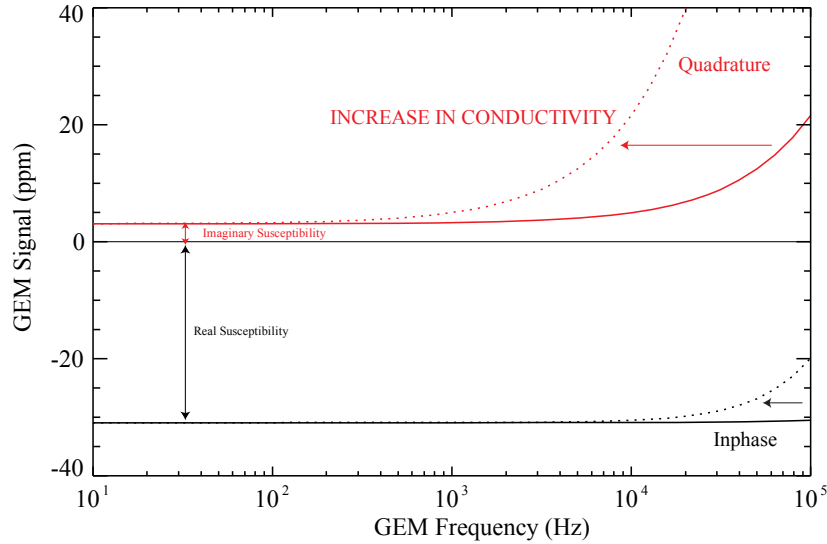


Figure 4-17 – Soil Model Response for the GEM-3 sensor. In-phase response is shown in red and quadrature response is shown in black. The solid lines represent a soil conductivity of 0.01 mho/m, the dashed lines 0.1 mho/m.

The in-phase measurements were not completely reproducible. There appears to be a general trend in height and frequency dependence, but the subtraction of the zero level does not appear to be working. One possibility is that the process of moving the GEM-3 from high in the air down to the shelf causes the in-phase zero level to shift irregularly. It is possible that small flexes in the sensor coil head is shifting the zero. For future measurements, it will be necessary to test this and see if the GEM-3 can be supported in some fashion to eliminate these shifts.

The measured in-phase signal is also not constant as a function of frequency below 10 kHz. There is a constant small slope across this frequency span. This frequency dependence is consistent with some proposed models for the behavior of soil magnetic susceptibility [7,11,12]. This model is described as a log-uniform distribution of magnetic relaxation times. The range of relaxation times is given by the model parameters of  $\tau_1$  and  $\tau_2$ . The frequency dependence of the susceptibility is given as:

$$\chi(\omega) = \chi_0 \left( 1 - \frac{1}{\ln(\tau_2/\tau_1)} \cdot \ln\left(\frac{i\omega\tau_2 + 1}{i\omega\tau_1 + 1}\right) \right)$$

If one assumes that the relaxation times are significantly above and below the bandwidth of the GEM-3 ( $\tau_1 < 10^{-7} s$  and  $\tau_2 > 0.1 s$ ) and apply this equation to the soil response calculation, one can match the sloped in-phase responses observed. Figure 4-18 plots the measured “Environmental Area” data versus model-based fits to the data (red and green curves). The slope in the in-phase is reasonably matched. Above 10 kHz, the in-phase signals tend to curve

downwards. Currently, there is no explanation of this. It will have to be explored further in future work.

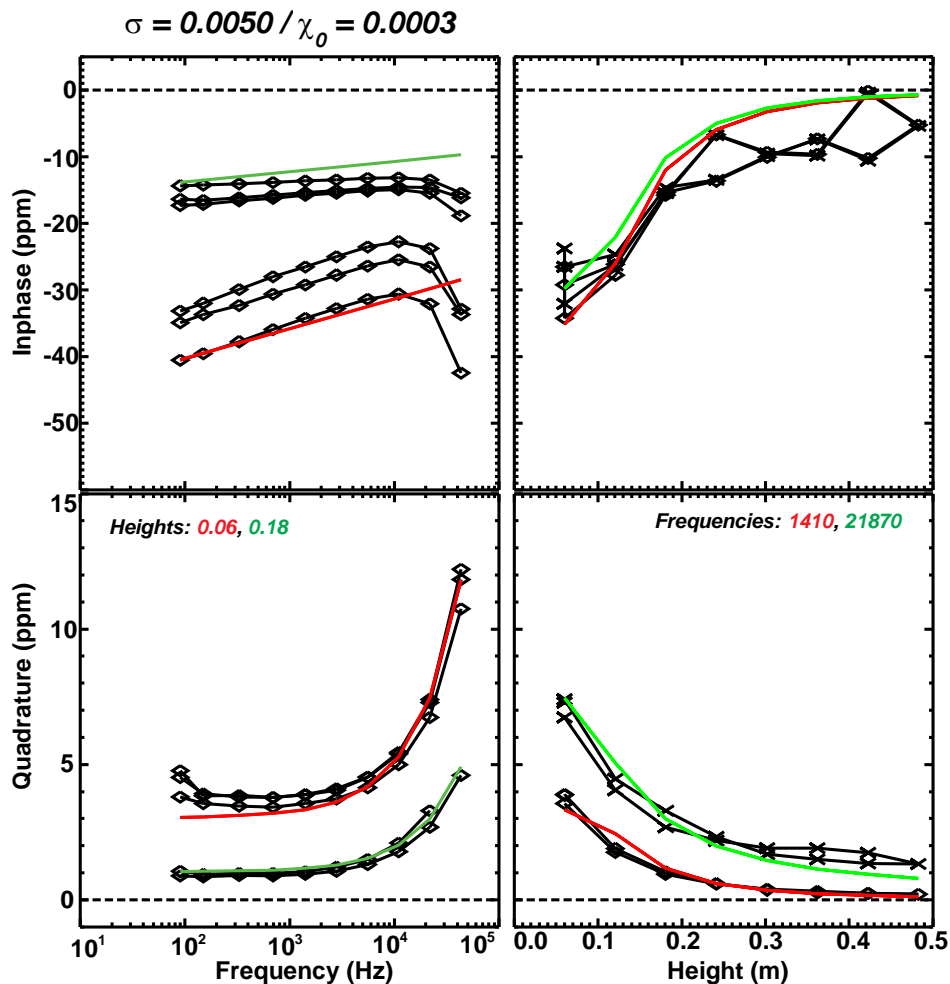


Figure 4-18 – Match of frequency dependent susceptibility model (red and green curves) to measured GEM-3 soil response (black curves and symbols) at the Environmental Area.

Overall soil parameters are presented in Table 4-2. Fitted soil conductivities are driven by the more stable quadrature measurement and range from 0.002 to 0.093 mho/m with the track measurements. The larger conductivities were at the “Boat Launch” site which was located next to and at a small elevation (less than 1 m) above the tidal Potomac River. Two additional measurements were taken on a sandy beach near the track; one at the water’s edge in saturated sand and one halfway up the beach on dry sand. As expected, increasing levels of conductivity were found. An unexpected result was noted in the surface offset parameter. Table entries flagged in red could only fit the quadrature data if the surface was shifted significantly lower than it really was. It appears that the model fits the data best based on the water level in the soil. The top dry layer of soil is ignored. Because of this, the fitted susceptibility parameters are larger than expected; since magnetic minerals are probably present in the top dry layer, but the model is trying to fit them deeper. The “Boat Launch” offsets of roughly 0.3 m are consistent with the soil moisture profiles in Figure 4-12. To fit these data more accurately, the data should be fit to a

layered model. It would be instructive to take soil cores to note depths where changes in soil type take place in the future.

Table 4-2 – Fitted Soil Model Parameters for the Blossom Point Test Areas

	Conductivity (mho/m)	Real Susceptibility (SI)	Imaginary Susceptibility (SI)	Surface Offset (m)	COMMENTS
<b>Boat Launch</b>		$\times 10^{-4}$	$\times 10^{-4}$		
1	0.093	<b>42</b>	<b>-0.59</b>	<b>0.262</b>	High Ground Along Rail Track
2	0.069	<b>44</b>	<b>-0.68</b>	<b>0.315</b>	High Ground Along Rail Track
3	0.32	7.9	-0.02	0.004	On Beach at Waterline
4	0.21	<b>12</b>	-0.04	<b>0.102</b>	On Beach above Waterline
<b>Environmental Area</b>					
1	0.005	2	-0.2	0.02	
2	0.0096	<b>12</b>	<b>-0.1</b>	<b>0.125</b>	
<b>L Range</b>					
1	0.0026	1.7	-0.085	0.01	
2	0.0021	0.9	-0.063	0.02	

Locations with a small fitted surface offset have real susceptibility values in the range of  $1 - 8 \times 10^{-4}$  and negative imaginary values that are 5-10% of the real value. The Bartington sensor measured real values in the range of  $10.0 \times 10^{-6} cgs$  which corresponds to  $1.2 \times 10^{-4}$  SI (units of soil model). The match is reasonable. The Bartington model used measures only the real susceptibility at a single frequency (0.958 kHz) and will not help with the indications from the GEM-3 of frequency dependent, complex values.

For the time domain sensors, the EM61 MkII and the EM63, there was no significant response to the soil observed for the rail/tower heights used. During the data analysis effort, this observed lack of response was revisited by making additional measurements with the EM61 MkII placed almost directly on the ground surface. To account for the unavoidable drift in the sensor response, the coils were alternately placed high in the air on plastic shelves (~ 2.0 m AGL) and then close to the ground on a single shelf (~ 0.05 m AGL). Because of the coil size, cable lengths, and the presence of the electronics package and backpack, these measurements were somewhat unwieldy to conduct. A different protocol for time-domain soil response measurements at small height increments close to the ground is recommended. One possibility is to use the time domain sensor developed under ESTCP MR-0601 which has several advantages and is discussed further in Section 6.1.1.

Figure 4-19 plots the EM61 MkII results on the Blossom Point test field near the pit used for overlapping signature measurements. The sensor was in the four time gate mode (no upper coil). The symbol/curves plot the measured data at four different heights. The y-axis on the right side indicates the response in manufacturer units of “milli-volts”. The amplitude of the signal in the first gate is on the order of 10 mV with the sensor only 0.10 m off of the ground. It is not surprising that there was no measurable signal at the rail height of 0.4 to 0.5 m with the EM63.

While the soil model used for evaluating the GEM-3 response can be applied to time domain sensors, its application to the EM61 MkII or EM63 sensors is, numerically, more involved. Our approach was to model the rectangular transmit coil as a sum of  $m$  by  $n$  dipoles and sum the field from these dipoles over the area of the receive coil. The soil response to a dipole can be found in [10]. A real conductivity and the frequency dependent complex susceptibility equation were included in the calculations. The response was calculated in the frequency domain and convolved with the FFT of the EM61 transmit pulse to get the time decay curve. The model results for the EM61 MkII are plotted as dashed curves in Figure 4-19 and scaled as voltage induced in the receive coil on the left side of the figure. In general [7], it has been noted that the time domain response is sensitive to the frequency dependence of the magnetic susceptibility. Based on an empirical model of this frequency dependence, the EMI response of weakly magnetic soil to a step function is expected to fall off as  $t^{-1}$ . The EM61 MkII measured and modeled response shows a similar, but not exact, dependence. The numerically modeled response to soil conductivity (for the range of values measured by the GEM-3, 0.002 to 0.1 mho/m) result in levels not measurable by the sensor. The curves fall off as  $t^{-5/2}$  and are rapidly lost in the sensor noise.

At a later date, a single sensor was borrowed from the MTADS Discrimination Array and used to measure the soil response on the Blossom Point test field. The results are shown in Figure 4-20. The TEM sensor has a 0.1 s base period with a 50% (bipolar) transmitter duty cycle and produces a transmit waveform that is much closer to a step function than the EM61 MkII (0.013 s base period and 25% duty cycle). The single sensor TEM curves, both measured and modeled, closely follow a  $t^{-1}$  decay. The TEM sensor measures the soil response over a much wider range of time gates, from less than 0.1 milliseconds out to 25 milliseconds. The TEM sensor output is also calibrated to the current output of the transmitter coil during the transmitter ON time.

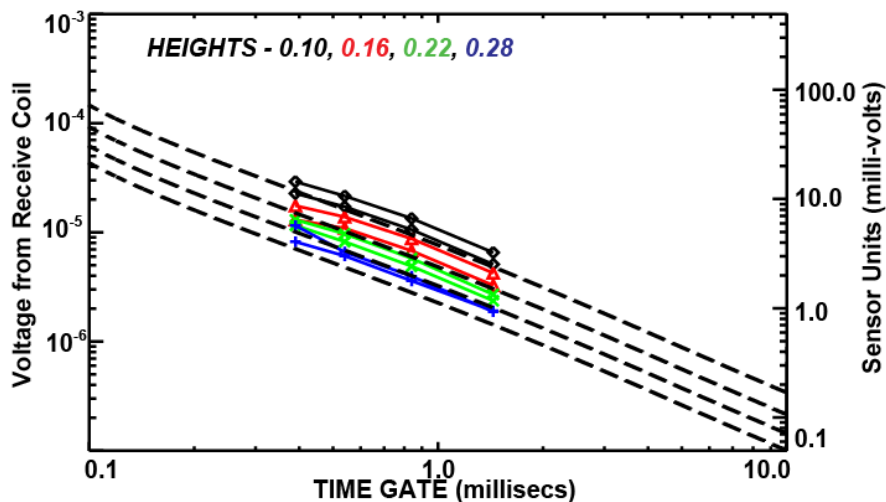


Figure 4-19 – Time-Domain Soil Response Measured using the EM61 MkII in 4-channel mode as a function of measurement height. The experimental data are shown as color-coded symbols and lines. The dashed lines represent the soil model discussed in the text as a function of sensor height.

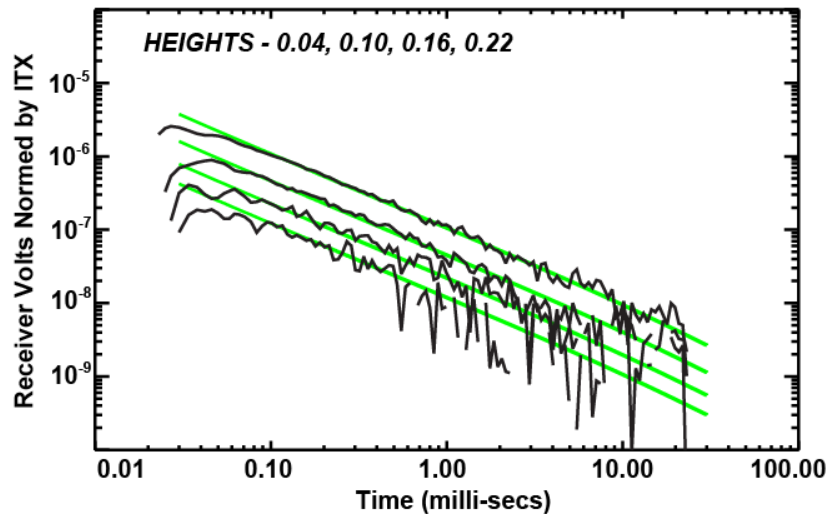


Figure 4-20 – Time-domain soil response measured and modeled using single sensor from MR-0601 TEM array as a function of measurement height. The black lines are the experimental data and the green lines represent the model results.

#### 4.6 Geolocation Uncertainties

Even in the absence of any background variation or sensor noise, sensor location uncertainties can degrade the classification performance of a sensor by degrading the quality of fitted parameter estimation from the survey data. In the majority of the classification approaches under investigation today, the resultant feature vectors are the inputs to the classification scheme. Increased uncertainty in these parameters directly translates into decreased classification performance.

A GPS antenna was mounted on our rail system tower. Measurements were made at three different heights above the ground and at two different speeds, fast and slow walking paces. The results are shown in Figure 4-21. As expected, a cm-level GPS system can do a consistently good job of tracking the position of the tower. RMS variations ( $1\sigma$ ) about the average track were on the order of stationary GPS variations, 0.007 m horizontal, 0.0162 m vertical. Larger relative errors and large, 1-2 m, systematic errors were observed when the number of GPS satellites was low ( $<6$ ) and when the signal SNR is degraded near obstructions such as a tree line.

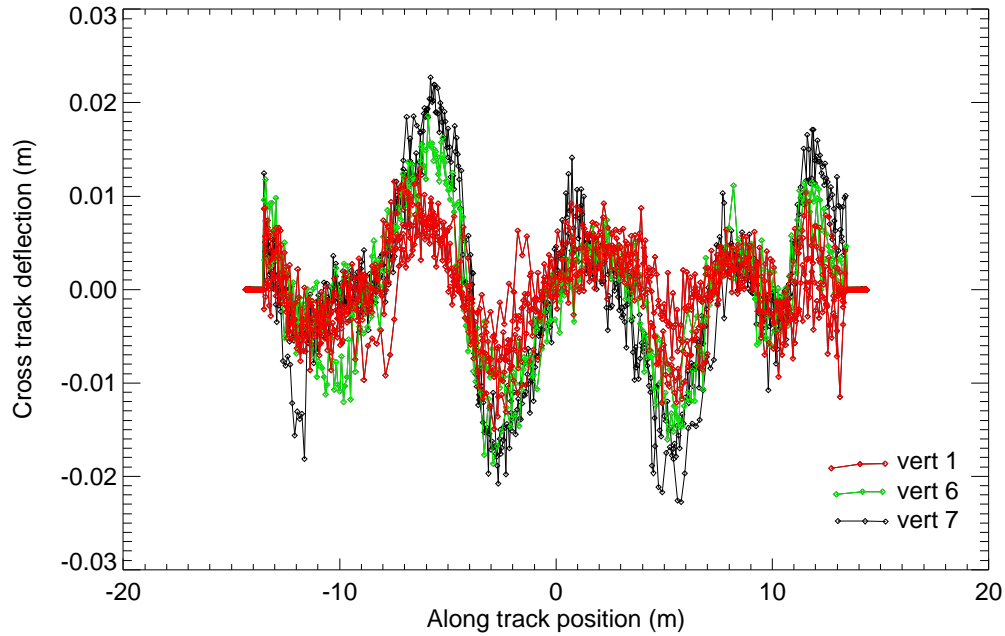


Figure 4-21 – Cross-track RMS variation of GPS position for a GPS position mounted on a rail system tower.

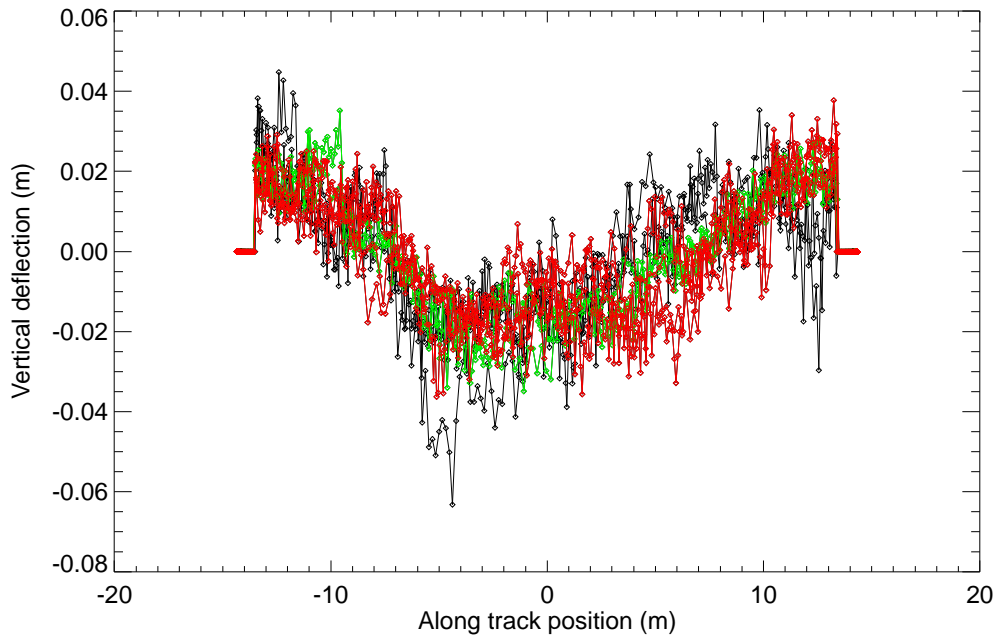


Figure 4-22 – Vertical RMS variation of GPS position for a GPS position mounted on a rail system tower.

#### 4.7 Blossom Point, MD – An Example Noise Budget

The goal of this project was to produce a method for determining a quantitative measure of the individual sources of noise or background levels and their total impact in an EMI sensor survey at a given site. The previous sections have discussed the measurement and quantification of

individual sources. In this section, the individual sources are combined to produce an overall estimate of the EMI noise budget for a site.

EMI sensor data were collected and averaged over three-second intervals and averaged for types of deployment platforms. The RMS variation (standard deviation) was calculated for each configuration. For the GEM-3 sensor, the towed platform was quieter than man-portable cart. The observer noise sources were different when comparing the in-phase and quadrature responses and vary with transmitter frequency. The results for both types of platforms are shown in Figure 4-23. In each panel, the data points and lines in black represent the noise levels of the GEM-3 when stationary.

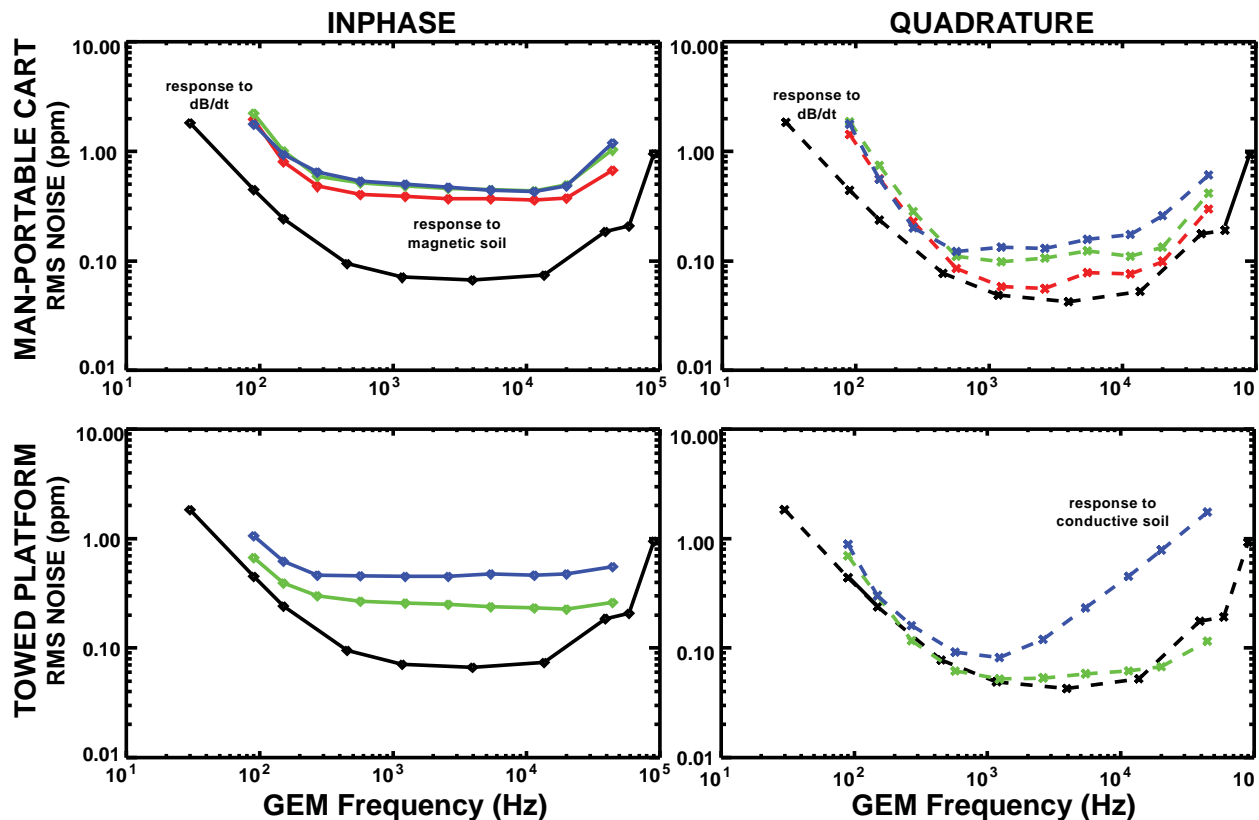


Figure 4-23 – Noise budgets for the GEM-3 sensor at Blossom Point, MD for towed-platform and man-portable deployment configurations. The noise floor for a stationary GEM-3 are shown in black.

A similar analysis for the EM61 MkII also shows that the towed platform is quieter than the man-portable cart configuration. The results are shown in Figure 4-24. Channels #1 - #3 represent different time gates for the lower receiver coil. Channel #4 represents the same time gate as Channel #1 but for the upper receiver coil. The noise levels range from 1 to 2 mV. The noise levels on the MP cart and towed platform decrease with the first three time gates. The upper coil/third time gate has larger noise levels than the lower coil/third gate due to more turns in the coil and possibly due to more motion related noise. The MP cart RMS noise level was greater than that for the towed platform. The L Range and Environmental Areas exhibited similar noise amplitudes, but the RMS noise level for the Boat Launch was significantly greater.

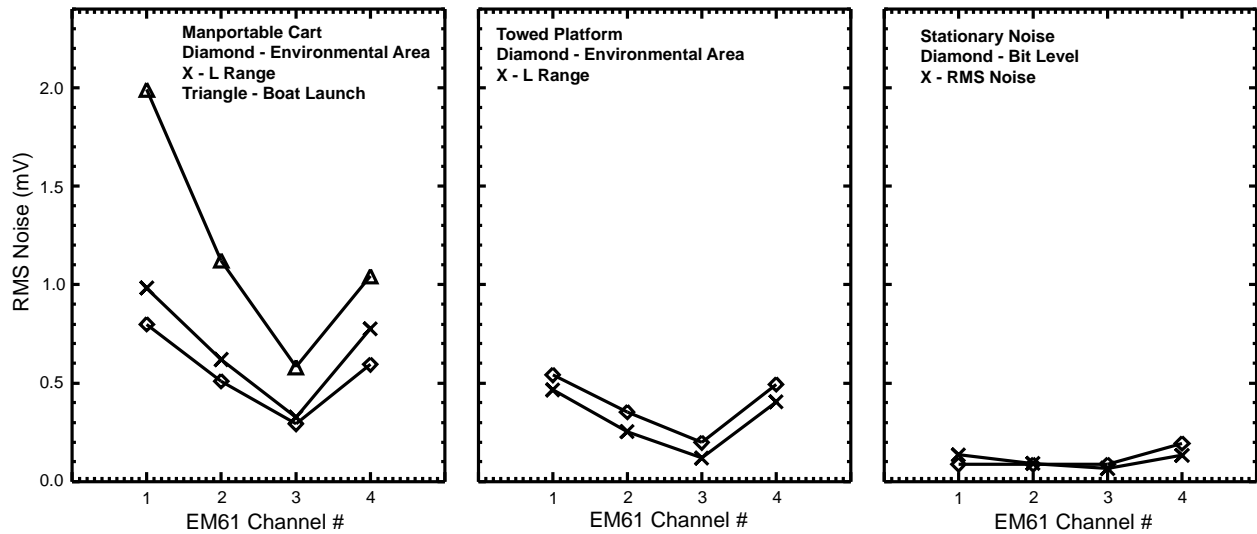


Figure 4-24 – Noise budgets for the EM61 MkII at Blossom Point, MD for towed-platform and man-portable deployment configurations. The noise floor for a stationary EM61 MkII are also shown.

## 5. Monte Carlo Study

### 5.1 Objective

As was shown in the previous section, it is difficult to completely separate the effect of an individual source of noise from the others, even under well controlled conditions. A software tool was developed to allow investigation of sources of noise in EMI surveys and to quantify their effects on detection probabilities and UXO/clutter discrimination success rates. That tool is described in this section. The tool is cast in terms of survey configuration parameters that may be altered by site operators, such as survey speed and lane spacing, and the effects of changing those parameters individually and in combinations.

### 5.2 The Monte Carlo Approach

The EM61 MkII Simulation Tool employs the Monte Carlo method [13]. We represent a complete UXO scenario using a stochastic model, including the buried target, survey platform, sensor, and data inversion process. Multiple realizations were then drawn from this model to estimate performance under various assumptions. This effort differed from previous work in that noise sources in the stochastic model are carefully grounded in data from controlled measurements made at Blossom Point as part of ESTCP project MR-0508, allowing separate noise mechanisms to be investigated individually and in concert. In particular, we have implemented new models to isolate sensor noise due to motion in the Earth's field, as well as motion relative to the ground. These improvements allow us to study effects from an increased range of scenarios, *e.g.*, different sensor height above ground, and different locations of the GPS receiver and sensor coils on the survey platform.

### 5.3 Modeling an EMI Survey Scenario

The analysis performed here may be repeated for any system in general, provided adequate knowledge of the sensor (e.g. time gate information for time-domain systems, or frequency information for frequency-domain systems), but in the current work, we studied the specific system shown in Figure 2-5. This wheeled cart platform incorporated a GPS receiver and IMU sensor rigidly mounted to the frame and it operates with various sensors including the GEM-3 and the EM61-MkII. We simulated this system moving at walking speeds over moderate terrain, based on data collected at Blossom Point MD. The cm-level GPS receiver and the IMU operate at data rates of 10 and 20Hz, respectively as described in Section 2.1.1.4. Monte Carlo simulations were run for both the GEM-3 and EM61-MkII configurations.

### 5.4 Stochastic Model

Each realization of the stochastic model is drawn in a sequence of five steps. The sequence is summarized in Table 5-1. Further details on each step can be found in Reference 16. After executing a large number of trials, overall performance is evaluated by comparing recovered values from Step 5 against the target definition specified in Step 1. Results of these trials are presented in following sections.

Table 5-1 – Steps of the Stochastic model

Step	Action
1	The target is defined. This includes position, orientation, and magnetic polarizability values (beta values).
2	The survey is defined. This includes the complete travel pathway for the sensor, including location and orientation (roll, pitch, yaw) at each measurement point.
3	Synthetic data are created. These are calculated using the dipole model outlined in Appendix B of Reference 16, given information from Steps 1 and 2. In the case of the EM61-MkII sensor, the dynamic response is incorporated into the forward model. In the case of the GEM-3, the dynamic response is negligible.
4	Observed data are created. These data include observed GPS values, IMU values, and sensor signals, all of which differ slightly from true GPS, IMU, and sensor signals established in Steps 2 and 3.
5	Observed data are inverted. Data from Step 4 are submitted to inversion using the same tools employed on real data from field surveys. Both static and dynamic inversion routines are used.

In the case of the EM61 MkII, the dynamic response of the sensor creates a significant spatial shift in the data. Figure 5-1 shows how dynamic response acts to shift data along-track and produce “chevron” patterns. A typical method of processing these data is to apply a time shift on the GPS position information until contours of the sensor signal appear to be aligned by eye. The data carving step is performed on these “aligned by eye” data. The data are then inverted in their shifted locations using a static inverter. However, after carving, the down-selected data are also returned to their true measurement locations for inversion with the dynamic inverter.

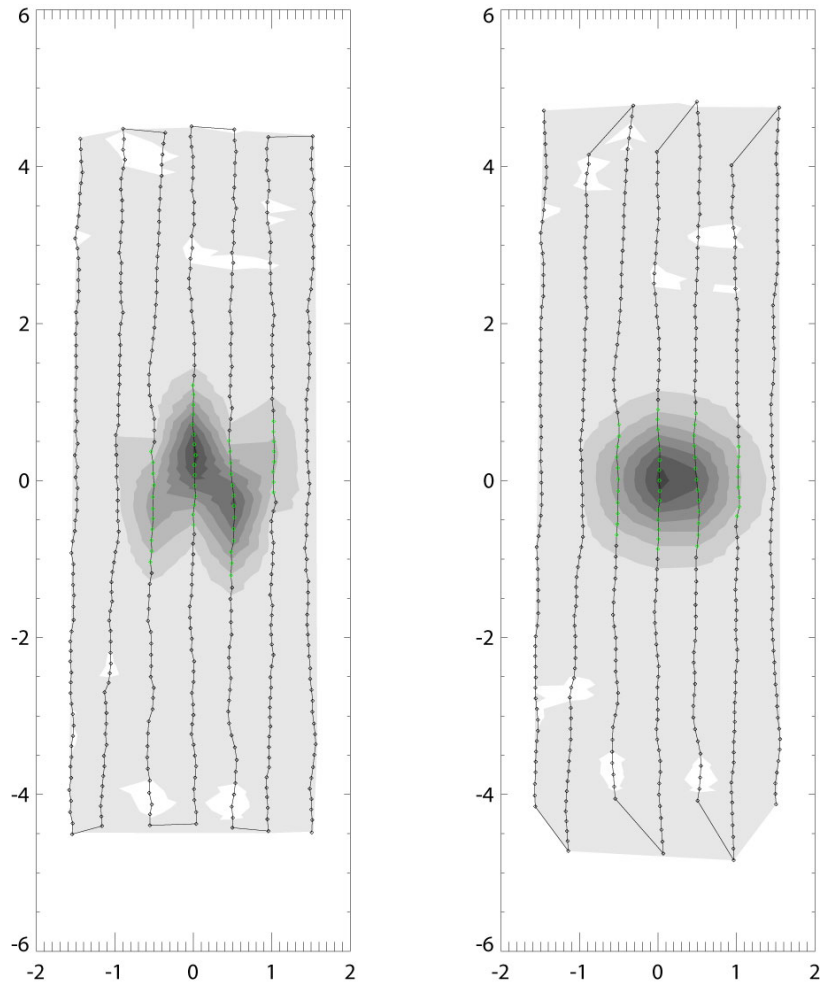


Figure 5-1 – Contour maps of synthetic EM61-MkII data, first time gate. The raw data (left image) shows the characteristic “chevron” pattern caused by the delayed onset of peak signals due to dynamic response of the sensor, which is moving at walking speed ( $\sim 1$  m/s). In the right image, a time lag is applied to the raw data, effectively shifting positions along-track until contours appear by eye to be aligned properly for further processing.

## 5.5 Simulation Results

Output from the simulator generally exhibits patterns of variability which are similar in scale and shape to variability seen on real surveys with similar hand-pushed cart vehicles, such as the EM61 MkII MP cart survey at Site 18 of the former Camp Sibert, AL. This comparison provides a real-world form of validation for our results comport.

Figure 5-2 shows a comparison of results from this Monte Carlo study against results obtained from a field survey at the former Camp Sibert, in which a wheeled EM61 MkII sensor was deployed. Figure 5-2 shows data for a large collection of 4.2-in mortars measured in the ground at the former Camp Sibert. These rounds will have some inherent variability from one example to the next, and the spread of recovered beta values must reflect this fact, while the synthetic sphere targets in our study were always identical, so we expect some differences in the recovered

beta clouds. There is also the fact that the 4.2-in mortars were a different shape, and larger than the ~6.5 inch spheres used in our study, and lastly, the terrain at Camp Sibert would produce different characteristic motion in the sensor platform, compared to motion at Blossom Point, which was the basis for our simulations. So we expect some differences, but we view the broad comparison favorably, and feel that it encourages a sense that our simulations are representative of reality.

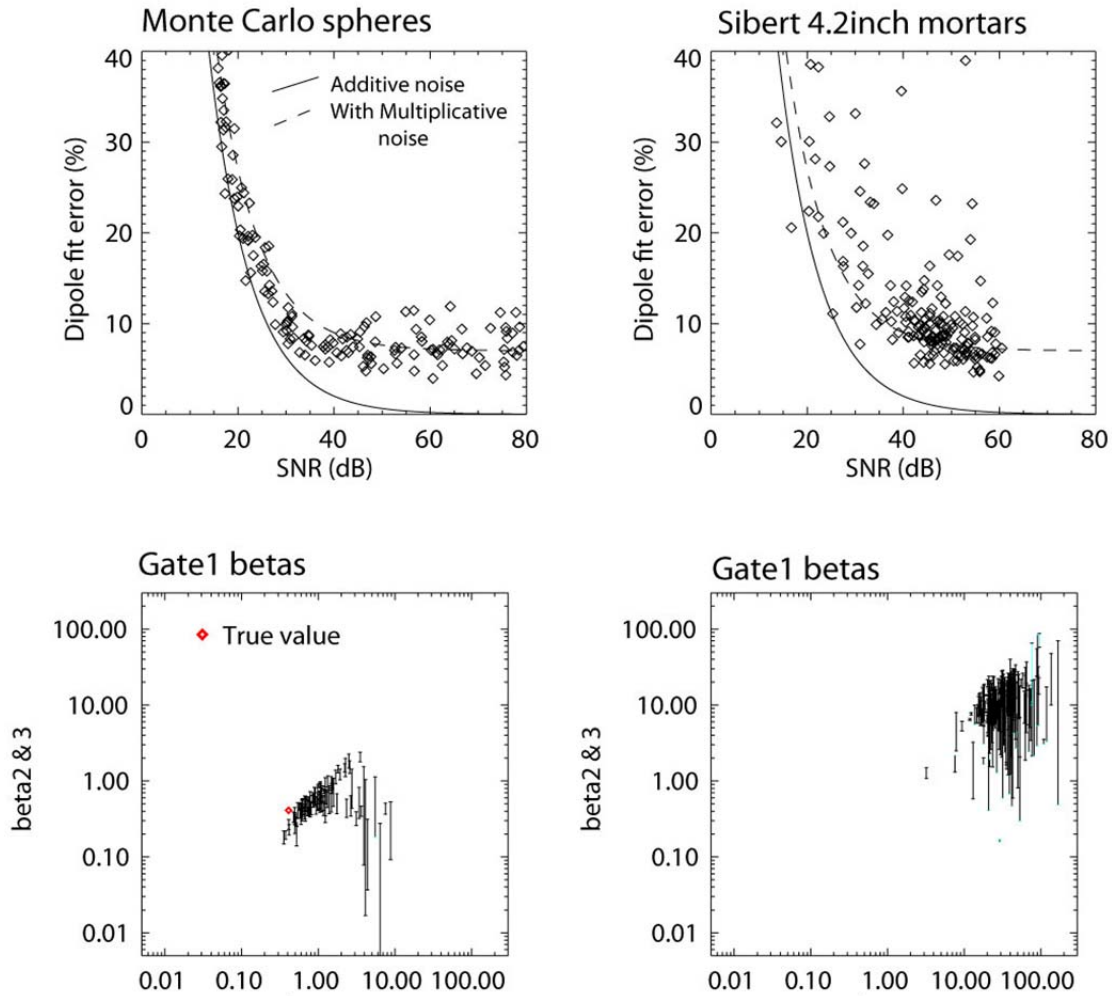


Figure 5-2 – Output from this Monte Carlo study (left two graphs) compares with corresponding results from Camp Sibert (right two graphs) in which a large number of 4.2-in mortars were processed. The upper set of graphs shows the relationship between fit error and signal to noise ratio (SNR). The lower set shows the spread of recovered beta values. This comparison is imperfect since the man-portable system deployed at the former Camp Sibert is different from the system modeled in this study (Figure 2-5). Still, the broad trends encourage a sense that these results are reasonable representations of reality.

#### *Additive noise vs. Multiplicative noise*

The upper two graphs in Figure 5-2 include a pair of lines drawn to illustrate the impact of additive noise and multiplicative noise. Additive noise refers to noise which is added on to the signal of interest, an example is B-dot noise. Multiplicative noise scales with the signal, an

example is navigation error, which produces large effects where signal gradients are steep, thus they scale with signal strength. The solid line represents theoretical performance in the presence of additive noise. Additive noise includes a variety of mechanisms and is generally site dependent. The amount of noise reflected by the solid line was adjusted to facilitate comparison on the graphs. The dashed line represents performance with both additive and multiplicative noise. Again, the amount of multiplicative noise here was chosen simply to facilitate comparison on the graphs. The equations for these theoretical performance curves are derived in Reference 14.

This Monte Carlo study assumed 6.5-in diameter sphere targets, which produce less response compared to the Sibert 4.2-in mortars, as evidenced in the lower two graphs. This study also assumed a wide range of burial depths for the targets, which is reflected in the wide distribution of SNR in the upper left graph, compared to a tighter grouping of SNR in the upper right graph.

Note that results in Figure 5-2 are generated without knowledge of IMU data, and using static inversion. This was done to simulate actual data processing implemented at real sites, as closely as possible.

#### *Dynamic response vs. Static response*

As discussed above, we implemented the standard static inversion approach, as well as a dynamic inversion. One interesting effect seen in these data is the clear bias in fitted target depth using the standard inversion procedure, but this bias is absent when dynamic response is incorporated. This effect can be understood since the dynamic response acts as a low-pass filter which tends to flatten sharply varying signatures (shallow targets) more than smoothly varying ones (deep targets). The effect of this distortion is to incorrectly fit shallow targets to deeper fitted depths, and assign high values to the response tensor to compensate for the increased range. This effect is most pronounced for shallow targets where sensor data include more high-frequency components and the low-pass filter thus has more effect.

#### *Lane spacing trade-off*

Figure 5-3 shows predicted performance under different lane spacing. These data apparently suggest there is little benefit in going to 0.25m lane spacing since results are comparable to 0.5m. Performance at 0.75m and 1m lane spacing are notably worse, which might allow decision-makers to weigh this trade-off more accurately when designing the survey.

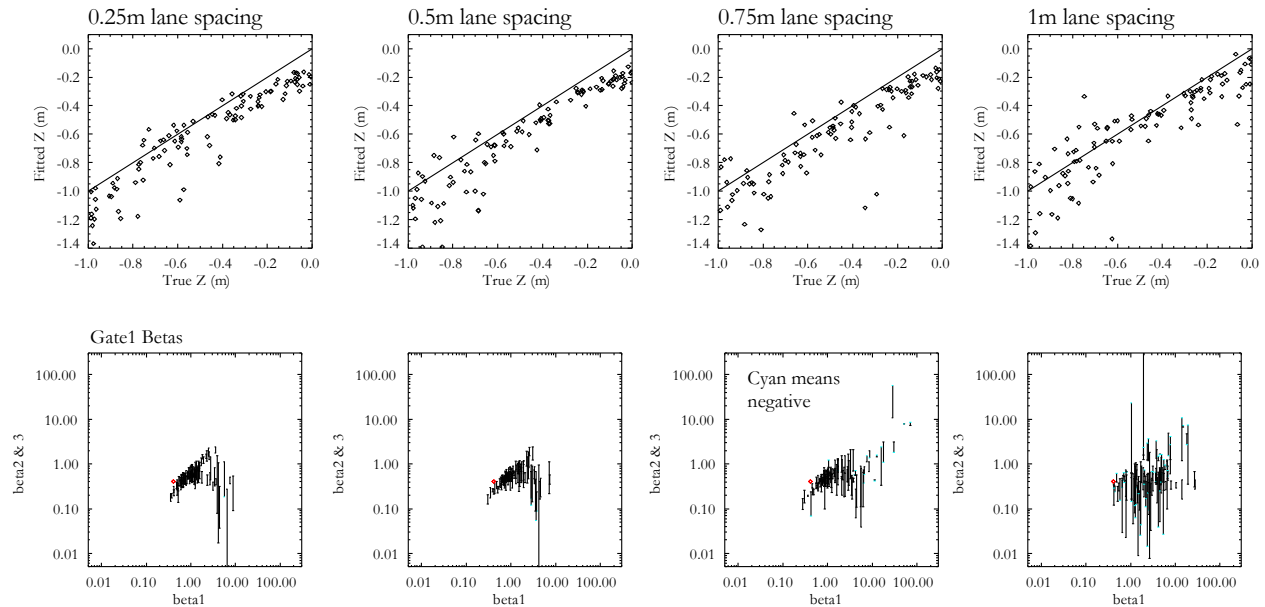


Figure 5-3 – Predicted performance with different lane spacings. The upper panels show the fitted  $z$  results and the lower panels plot  $\beta_2$  and  $\beta_3$  versus  $\beta_1$ . The solid line in the upper panels indicates where the fitted  $z$  equals the true  $z$  value.

#### *Trade-offs for other configurations*

Figure 5-4 shows predicted performance under different survey configurations. If the sensor is placed with 0.5m height above the ground instead of 0.25m, there is an associated degradation in performance. We also expect degraded performance when the sensor is too close to the ground due to heightened geologic noise, and this tool would allow determination of an optimal height, when applied to a specific sensor and site.

Figure 5-4 also shows the performance benefit gained by including IMU signals in the inversion, as well as benefit gained by simply mounting the GPS receiver directly over the sensor instead of having it positioned toward the rear of the platform. The improvement in performance results from removing the horizontal lever arm, which contributes navigation errors through interaction with imperfect yaw data.

Note that all the results in Figure 5-4 illustrate the same bias for depth errors, which is accentuated at shallow depths. This effect is due to the low-pass filter aspect of the sensor dynamic response, as discussed above in “Dynamic response vs. Static response”.

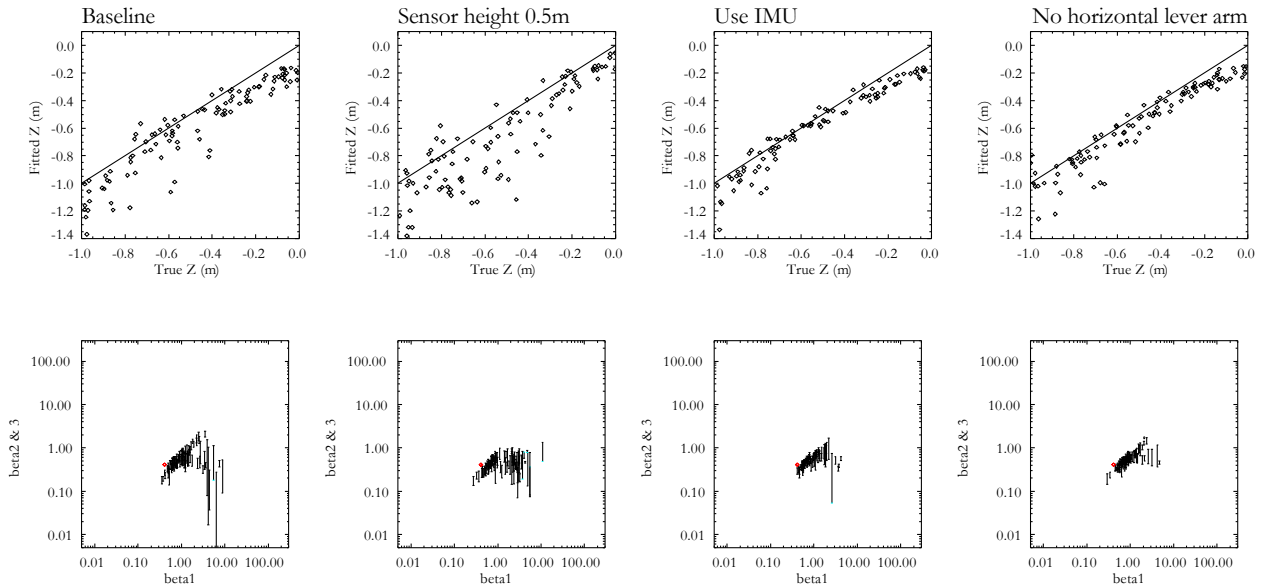


Figure 5-4 – Predicted performance for other survey configurations. The upper panels show the fitted z results and the lower panels plot  $\beta_2$  and  $\beta_3$  versus  $\beta_1$ . The solid line in the upper panels indicates where the fitted z equals the true z value.

## 6. Implementation at a New Site

Based on the presented modeling results and analysis, we outline below two proposed strategies for characterizing the EMI noise budget at a new site. The first strategy is a full set of measurements and analysis to be conducted over the course of a week. The second involves the use of our EM61 MkII Simulation Tool. From these results, one can begin to understand real world EMI survey noise sources both individually and in combination. One can start to quantify these effects in terms of survey configuration parameters which are under site manager and data collection operator control, such as lane spacing and survey mode.

### 6.1 Full-Scale EMI Noise Characterization Demonstration

This strategy's level of effort is designed to require approximately 1 week of data collection with a staff of 6 people. The following sections discuss the proposed suite of measurements and the set of EMI sensors required to make those measurements.

#### 6.1.1 EMI Sensors

Individual samples of the three EMI sensor types discussed in Section 2.1.1 were characterized at length during this project. The Geonics EM61 MkII sensor is the de facto standard instrument used in the UXO industry. The Geophex GEM-3 sensor has yielded significant information on geological response in this effort and the data products have proved amenable to separating the contributions of the noise sources studied. The richness of results from the GEM-3 more than compensate for the sensor's limited penetration into the UXO industry. The GEM-3 is also the only frequency-domain EMI sensor examined in this demonstration.

The Geonics EM63 sensor is a time-domain instrument like the EM61 MkII, but samples a larger portion of the signal transient (180  $\mu$ s – 25 ms versus 216  $\mu$ s – 1.27 ms for the EM61 MkII) with more points (26 versus 3/4 points). The value of sampling the signal transient at later times is demonstrated in Figure 6-1, where data from the MTADS Discrimination Array (built under ESTCP Project MR-0601 [15]) are shown for UXO and cultural items.

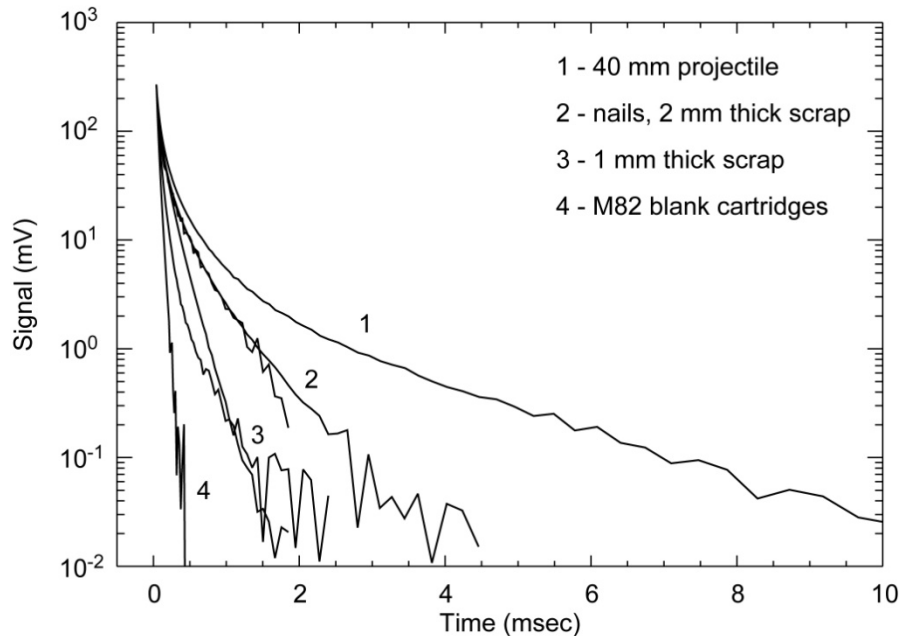


Figure 6-1 – MTADS Discrimination Array Transients for Several Items

The EM61 MkII can only sample the sample transient out to 1.27 ms, where the transients for the four items shown in Figure 6-1 are still very similar and would be difficult to separate. After 2 ms, the thin-walled items are clearly separated from the heavier walled items. As discussed in Section 4.4, the frequency-dependent geologic responses measured with the GEM-3 sensor increase in the quadrature response as a function of frequency. The first time gate of the EM63 is at 177  $\mu$ s, and corresponds roughly to a GEM-3 frequency of 1 kHz. Later EM63 time gates correspond to lower GEM-3 frequencies. The lack of a measured geological response in the data collected with the Geonics sensors is consistent with the trends of the GEM-3 measurements. A time-domain sensor capable of sampling the signal transient earlier is likely required to resolve any geological response in the time domain.

The EM63 is a heavy instrument with masses of 32 kg, 4.5 kg, 10 kg, for the sensor, console, and battery pack, respectively. The EM61 MkII masses 22 kg total for reference, 14 kg for the sensor and 8 kg for the backpack (electronics and battery). Given the signal drift rates associated with EM63 and the data collection protocols required to overcome these drift rates and the physical stresses of making these measurements, a significantly lighter, preferably lower-drift rate sensor is required to make reasonable TEM geological response measurements.

Fortunately, such a sensor has recently become available. The TEM sensor developed by G&G Sciences for the MTADS Discrimination Array (ESTCP MR-0601) is significantly lighter than the EM63 (2.5 kg) and similar in size and weight to the EM61 MkII-HH and the GEM-3

handheld models. The coils are wound on concentric stiff foam cores using a square coil design, with transmitter and receiver coil widths of 35 and 25 cm, respectively. The coils are wound in a non-overlapping pattern which leads to a coil height of 8 cm. Figure 6-2 shows an example of the completed coil assembly. The full decay curve can then be measured from 40  $\mu$ s to beyond 10 ms with a sampling rate of 500 kHz. The recorded transients are either recorded as all points or binned into approximately 120 time gates. A lightweight amplifier is collocated with the coil assembly, increasing the maximum cable run to the electronics to at least 7m. At this time, the electronics and transmitter from the MTADS Discrimination Array can operate the sensor but an ESTCP-funded project to develop a handheld version is currently under way (ESTCP Project MR-0807) which can be used as a complete, compact unit. The existing Discrimination Array electronics may also be configured to act as an external background monitor, using the array's high-bandwidth D/A electronics. The system's 500 kHz bandwidth is more than double that of the NRL Low Frequency Spectrum Analyzer and provides a high-quality amplifier to boost the recorded signal.

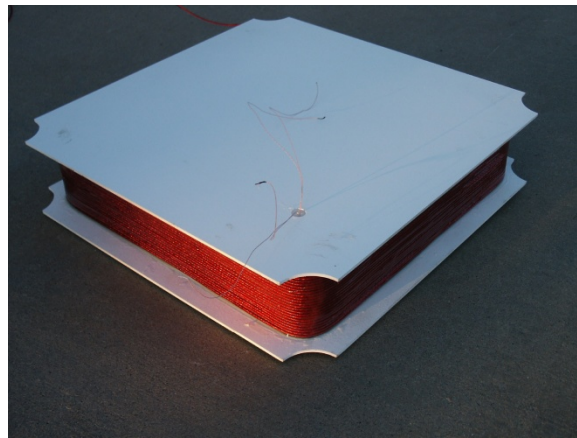


Figure 6-2 – EMI sensor developed during ESTCP MR-0601



Figure 6-3 – Handheld TEM sensor developed for ESTCP MR-0807 in the field

Based on the quality and scope of the data that can be collected with the MR-0601 sensor, it is recommended that the MR-0601 replace the EM63 in future demonstrations for this project.

### **6.1.2 Measurements**

Upon selection of a new site, 3 – 4 unique areas, or traverses, with at least 30m of usable area each should be selected for study. Soil moisture and magnetic susceptibility measurements along each traverse with standard instrumentation is recommended following the protocols outlined in Section 3.6 of Reference 16. The impact of external noise sources should be monitored using the GEM-3 and MR-0601 sensors. If a strong external noise source is identified such as a power line, additional measurements as a function of distance should be made with the GEM-3 and EM61 MkII to characterize the effects.

The geological response is to be characterized with two methods along each traverse. The horizontal structure of the geological response will be measured with the GEM-3 and EM61 MkII sensors mounted on a MP cart. At selected stations along each traverse that are free of compact anomalies, the vertical structure of the geological response will be determined using the modified procedure discussed in Section 4.4 using the GEM-3 and the MR-0601 sensors.

Motion-induced noise should be characterized for the intended modes of operation for the EMI sensors on site. The data sets collected for the horizontal structure of the geological response will provide continuity with existing data. The addition of cm-level GPS and higher bandwidth IMU measurements will facilitate these measurements and are recommended.

### **6.1.3 Deliverables**

The data collected during such an effort will be analyzed, the unique noise characteristics of the site determined, and a site-specific guidance document generated. Comparison to past studies (initially to Blossom Point) will allow site managers and data collectors to make informed decisions about the appropriateness of the various sensor technologies on the site and the noise floor limitations on anomaly detection and classification.

## **6.2 EM61 MkII Simulation Tool Demonstration**

A scaled-back version of the proposed effort more tightly focused on the ubiquitous EM61 MkII sensor potentially offers a higher benefit to cost ratio and more general applicability to the UXO community as a whole. One half day's measurements are proposed to be coupled with an active EM61 MkII survey effort. These measurements could be helpful to survey data collectors and to the regulatory community. The inclusion of the dynamic response of the sensor does appear to have an impact on the overall performance of the data collection and processing methodology. Evaluation of the dynamic response impact on data from the site could guide the decision to use more advanced analysis methods or not.

### **6.2.1 EMI Sensors**

As stated above, EM61 MkII sensor is the de facto standard instrument used in the UXO industry. This measurement strategy is envisioned to be as “bolt-on” to an existing effort as possible. The EM61 MkII and the positioning system (e.g. cm-level GPS) planned for the

production effort would be used. A high-bandwidth IMU ( $\geq 25$  Hz rolloff) would be added to the survey platform to measure the platform orientation. If it is not feasible to include an IMU, orientation information from another appropriate source could be used if desired to estimate the effect of platform motion for the site, with the associated cost of degraded fidelity. A test coil with a switched contact would be used to measure the dynamic response parameters for the specific EM61 MkII(s) to be used. A canonical test object with a well-characterized sensor response such as an Aluminum sphere would be used as well.

### **6.2.2 Measurements**

Six classes of measurements would be made in the course of a half day. A long set (approximately 1 hour) of stationary data would be collected with the entire system (EM61 MkII, GPS, and IMU) previously warmed up and running. Several long transects would be surveyed with the entire system. Five to ten profiles, both horizontal and vertical in orientation, would be collected to characterize the soil response at the site. At three different heights above the ground, static calibration measurements would be made with the canonical object. Dynamic calibration measurements would be made by passing the system many times (approximately 10) over the canonical object placed on a hard-packed, flat surface. Non-reinforced pavement would be acceptable for these measurements. The dynamic response parameters would be determined for the specific EM61 MkII(s) using the switched test coil.

### **6.2.3 Deliverables**

The deliverables from this effort would be an evaluation of the site-specific noise characteristics of the site and the EM61 EMI sensor, both in general and specifically for the tested units, for the classification of UXO items on the site. Additionally, the value added of using advanced modeling techniques such as dynamic inversion for data collected on site can be evaluated.

## 7. References

1. "Report of the Defense Science Board Task Force on Unexploded Ordnance," December 2003, Office of the Under Secretary of Defense for Acquisition, Technology, and Logistics, Washington, D.C. 20301-3140, <http://www.acq.osd.mil/dsb/uxo.pdf>.
2. "Operating Instructions, EM61MK2 Data Logging System for Field Computer Allegro Field PC, EM61MK2A, v2.20," Geonics, Ltd., February 2005.
3. Geologic Map of Charles County, Maryland, McCartan, Lucy, 1989, Maryland Geological Survey.
4. "Electromagnetic Induction and Magnetic Sensor Fusion for Enhanced UXO Target Classification," H.H. Nelson and B.J. Barrow, NRL/PU/6110—00-423, September 15, 2000.
5. "Frequency Domain Electromagnetic Sensors for the Multi-sensor Towed Array Detection System," H.H. Nelson, B.J. Barrow, T.H. Bell, R.S. Jones, B. San Filipo, and I.J. Won, NRL/MR/6110—02-8650, November 27, 2002.
6. "Demonstration of Basalt-UXO Discrimination by Advanced Analysis of Multi-Channel EM63 Data at Kaho'olawe, Hawaii," G.H. Ware, W.F. Tompkins, H.A. Ware, K.E. Lemley, and A.Z. Kostera, Proceedings of the UXO/Countermining Forum 2002, September 3-6, 2002, Orlando, FL.
7. "Effects of Soil Electromagnetic Properties on Metal Detectors," Y. Das, IEEE Trans. Geosci. Remote Sens., vol. 44, no. 6, pg. 1444-1453, June 2006.
8. "A multidisciplinary analysis of frequency domain metal detectors for humanitarian demining," C. Bruschini, Ph.D. dissertation, Vrije Univ., Brussels, Belgium, 2002.
9. "Interpretation Theory in Applied Geophysics," F. S. Grant and G. F. West, McGraw-Hill, New York, 1965.
10. M. N. Nabighian, Ed., Electromagnetic Methods in Applied Geophysics, ser. Investigations in Geophysics no. 3. Tulsa, OK: Soc. Explor. Geophys., 1987, vol. 1 and 2.
11. S. Chikazumi, Physics of Magnetism. New York: Wiley, 1964.
12. "The effect of a superparamagnetic layer on the transient electromagnetic response of a ground," T. Lee, Geophys. Prospect., vol. 32, pp. 480-496, 1984.
13. "Chapter 12: Monte Carlo Methods for System Quantification" in *Reliability Engineering and Risk Assessment*, E.J. Henley and H. Kumamoto, Prentice Hall (1981).
14. "Processing and Analysis Results for MR-1310 Blossom Point Demonstration," Jim Kingdon and T.H. Bell, SAIC Technical Report for MR-1310.

15. "EMI Array for Cued UXO Discrimination, ESTCP MR-0601, Cost and Performance Report," D.C. George, J.B. Kingdon, T. Furuya, D.A. Keiswetter, T.H. Bell, G.R. Harbaugh, and D.A. Steinhurst, NRL Memorandum Report NRL/MR/6110—11-9317, Naval Research Laboratory, Washington, DC, February 7, 2011.
16. "Quantification of Noise Sources in EMI Surveys, Technology Demonstration Report, Army Research Laboratory Blossom Point, Maryland, July – September, 2006," G.R. Harbaugh, D.A. Steinhurst, M. Howard, B.J. Barrow, J.T. Miller, and T.H. Bell, NRL Memorandum Report NRL/MR/6110—10-9235, Naval Research Laboratory, Washington, DC, January 14, 2010.

## 8. Points of Contact

POINT OF CONTACT	ORGANIZATION	Phone/Fax/email	Role in Project
Dr. Jeff Marqusee	ESTCP	Tel: 703-696-2120	Director, ESTCP
		Fax: 703-696-2114	
		Jeffrey.marqusee@osd.mil	
Dr. Anne Andrews	ESTCP	Tel: 703-696-3826	Deputy Directory, ESTCP
		Fax: 703-6962114	
		Anne.andrews@osd.mil	
Dr. Herb Nelson	ESTCP	Tel: 703-696-8726	Program Manager Munitions Response
		Fax: 703-696-2114	
		Herbert.nelson@osd.mil	
Ms. Katherine Kaye	HydroGeoLogic, Inc.	Tel: 410-884-4447	Program Manager Assistant Munitions Management
		kkaye@hgl.com	
Dr. Dan Steinhurst	Nova Research, Inc.	Tel: 202-767-3556	Senior Staff Scientist Co-PI of Project
		Fax: 202-404-8119	
		Cell: 703-850-5217	
		dan.steinhurst@nrl.navy.mil	
Mr. Glenn Harbaugh	Nova Research, Inc.	Tel: 301-392-1702	Site Safety Officer
		Fax: 301-392-1702	
		Cell: 804-761-5904	
		roo749@yahoo.com	
Dr. Tom Bell	SAIC – ASAD	Tel: 703-414-3904	Chief Scientist Co-PI of Project
		thomas.h.bell@saic.com	
John Breznick	NAEVA Geophysics, Inc.	Tel: 434-978-3187	General Manager
		Cell: 434-825-8175	
		Fax: 434-973-9791	
		jbresnick@naevageophysics.com	
Jack Kaiser	Army Research Laboratory Blossom Point Facility	Tel: 301-870-2329	Facility Operations Specialist
		Fax: 301-870-3130	
		Cell: n/a	
		jkaiser@arl.army.mil	